Volume 15
Number 3
21 January 2024
Pages 783–1164

Chemical Science

rsc.li/chemical-science

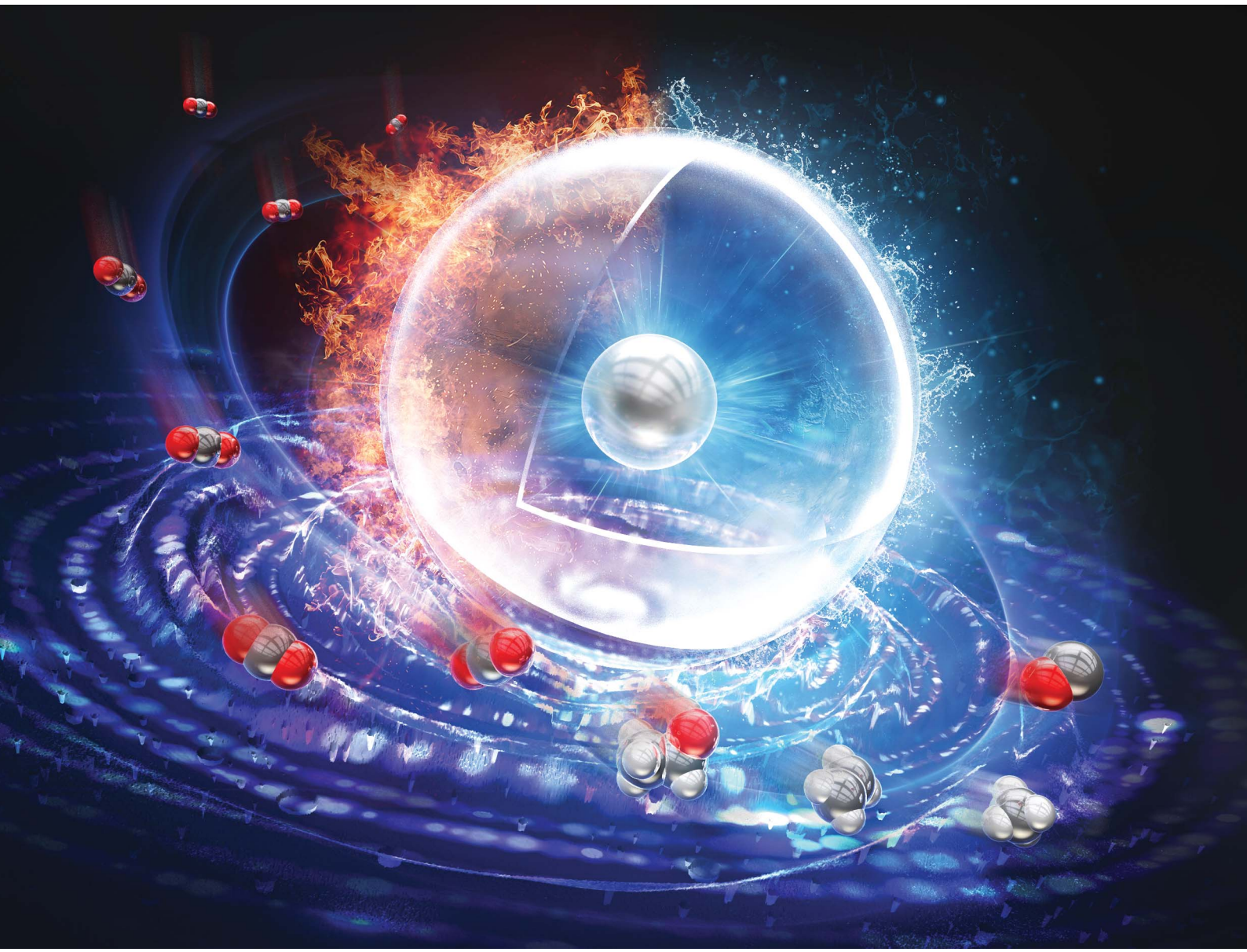

ISSN 2041-6539

ROYAL SOCIETY OF CHEMISTRY

REVIEW ARTICLE
Yasutaka Kuwahara, Hiromi Yamashita *et al.*
Hollow carbon-based materials for electrocatalytic and thermocatalytic CO_2 conversion

Chemical Science

ROYAL SOCIETY OF CHEMISTRY

REVIEW

View Article Online
View Journal | View Issue

Cite this: *Chem. Sci.*, 2024, **15**, 854

Hollow carbon-based materials for electrocatalytic and thermocatalytic CO_2 conversion

Kaining Li,[a] Yasutaka Kuwahara *[ab] and Hiromi Yamashita *[ab]

Electrocatalytic and thermocatalytic CO_2 conversions provide promising routes to realize global carbon neutrality, and the development of corresponding advanced catalysts is important but challenging. Hollow-structured carbon (HSC) materials with striking features, including unique cavity structure, good permeability, large surface area, and readily functionalizable surface, are flexible platforms for designing high-performance catalysts. In this review, the topics range from the accurate design of HSC materials to specific electrocatalytic and thermocatalytic CO_2 conversion applications, aiming to address the drawbacks of conventional catalysts, such as sluggish reaction kinetics, inadequate selectivity, and poor stability. Firstly, the synthetic methods of HSC, including the hard template route, soft template approach, and self-template strategy are summarized, with an evaluation of their characteristics and applicability. Subsequently, the functionalization strategies (nonmetal doping, metal single-atom anchoring, and metal nanoparticle modification) for HSC are comprehensively discussed. Lastly, the recent achievements of intriguing HSC-based materials in electrocatalytic and thermocatalytic CO_2 conversion applications are presented, with a particular focus on revealing the relationship between catalyst structure and activity. We anticipate that the review can provide some ideas for designing highly active and durable catalytic systems for CO_2 valorization and beyond.

Received 25th September 2023
Accepted 5th December 2023

DOI: 10.1039/d3sc05026b

rsc.li/chemical-science

1. Introduction

The rapid advancement of industrialization has led to high fossil-fuel consumption, causing an ever-increasing atmospheric CO_2 concentration. Excessive CO_2 emissions are the main contributors to global warming and the resulting abnormal climatic variation, glacial ablation, ecosystem destruction, *etc.*,[1,2] which seriously threaten the shared future of mankind. In the past decades, many efforts have been devoted

[a]*Division of Materials and Manufacturing Science, Graduate School of Engineering, Osaka University, 2-1 Yamada-oka, Osaka 565-0871, Japan. E-mail: kuwahara@mat.eng.osaka-u.ac.jp; yamashita@mat.eng.osaka-u.ac.jp*

[b]*Innovative Catalysis Science Division, Institute for Open and Transdisciplinary Research Initiatives (OTRI), Osaka University, 2-1 Yamada-oka, Suita, Osaka 565-0871, Japan*

Kaining Li

Kaining Li received his MS degree in Environmental Chemistry from South-Central University for Nationalities in 2021. He is pursuing a PhD degree from the Graduate School of Engineering, Osaka University, under the supervision of Prof. Hiromi Yamashita. His current research interests are novel nanomaterials and their applications in catalytic CO_2 conversion.

Yasutaka Kuwahara

Yasutaka Kuwahara received his PhD degree in engineering from Osaka University in 2011. He was a researcher at National Institute of Advanced Industrial Science and Technology (AIST), Japan, in 2012–2014. He was appointed as an assistant professor at Osaka University in 2014, and has been an associate professor since 2021. His current research interests include the design of nanostructured catalysts with multi-functionalities using porous materials and their applications to green chemical reactions and the valorization of CO_2.

to controlling the CO_2 concentration worldwide (*e.g.*, adoptions of the Kyoto Protocol and the Paris Agreement). The objective of the Paris Agreement is to keep the global average temperature below 2 °C above the pre-industrial mean, with a temperature increase of 1.5 °C limit.[3,4] Nevertheless, the current trend of anthropogenic CO_2 growth makes achieving this goal an urgent task for a sustainable community and economic society.[5]

Catalytic CO_2 reduction conversions (*e.g.*, photocatalysis, thermocatalysis, and electrocatalysis) to produce high-value-added fuels and feedstocks, offer a promising means of realizing carbon neutrality and potentially help to mitigate the global warming issue.[6–9] In comparison to photocatalysis, thermal catalytic and electrocatalytic CO_2 conversions are easier to scale up, due to the appropriate reaction kinetics and lack of dependence on the availability and cost of high-intensity light sources. Herein, our review mainly focuses on these two reactions.

Electrochemical CO_2 reduction reaction (eCO_2RR), powered by electrical energy, refers to the process of using electrochemical cells to convert CO_2 to valuable compounds, such as carbon monoxide (CO), methane (CH_4), methanol (CH_3OH), ethylene (C_2H_4), *etc.* A typical electrocatalytic CO_2 reduction reaction involves four main steps:[10,11] (1) diffusion of CO_2 to the electrolyte/cathode interface; (2) CO_2 molecules are adsorbed on the cathode surface; (3) when an external bias is applied, the oxygen evolution takes place at the anode due to the water oxidation, and the generated electrons are then transferred to the cathode through an external circuit, where they can participate in the CO_2 reduction processes; (4) desorption of final products from the cathode. These steps jointly determine the overall efficiency of eCO_2RR. Recently, eCO_2RR has become the research hotspot in CO_2 utilization owing to its multifarious advantages, including mild operation conditions (room temperature and atmospheric pressure), flexible reactor platforms, and relatively high conversion efficiency.[12–16] Integrating renewable energy with eCO_2RR, simultaneously achieving a net CO_2 reduction and chemical raw material supply is possible. Despite eCO_2RR possesses numerous advantages, its pragmatic commercialization is still confronting great challenges. Firstly, as a chemically inert and thermodynamically stable molecule, CO_2 is difficult to be activated because of the stable C=O bond (806 kJ mol^{-1});[17,18] thus, a high potential is inevitably needed to drive the eCO_2RR. Secondly, most eCO_2RR can yield multiple products, which makes the direct utilization of products difficult, requiring an extra target product separation process. Third, noble metal-based catalysts (Au, Ag) usually deliver high electroactivity, but are less desirable considering their cost-efficiency and scarcity. For these reasons, efficient electrocatalysts with the characteristics of highly exposed active sites, good conductivity, abundant pore structure for target molecule transfer, and high earth-abundance are urgently needed.[19,20]

Thermocatalytic CO_2 conversion, mainly including CO_2 hydrogenation and CO_2 dry reforming of methane (DRM), is a feasible process to alleviate the large CO_2 emissions from the viewpoint of cost-efficiency.[21] Among them, DRM is a highly endothermic reaction with the equation $CH_4 + CO_2 \rightarrow 2CO + 2H_2$, $\Delta H^\circ = 247$ kJ mol^{-1}.[22] The large energy consumption and the deactivation of catalysts caused by active metal sintering or coke deposition during the DRM process seriously hindered its applicability. Compared to DRM, thermal hydrogenation of CO_2 shows a lower thermodynamic limitation, which involves the reaction of CO_2 and H_2 and can afford high levels of variety and tailorability for the production of desirable hydrocarbons and oxygenates.[23,24] Conventionally, the catalytic performance and product selectivity highly depend on the catalyst. Accordingly, the development of CO_2 hydrogenation catalysts with high CO_2 adsorption and activation ability, robust stability, and good selectivity, is of great practical relevance.

In nature, cells with hollow structures are the fundamental unit of an organism, and this unique structure endows them with distinctive properties that allow for the adjustment of adsorption, separation, and exchange for substrates required to maintain vital life activities.[25,26] Inspired by nature, many encouraging hollow-structure nanoreactors have been developed for energy storage,[27–31] biomass conversion,[32,33] and environmental catalysis applications.[34,35] In recent years, hollow-structured carbon (HSC) and its derived nanomaterials have attracted considerable attention in the fields of thermocatalysis and electrocatalysis for CO_2 conversion due to their advantageous features. Firstly, guest molecules and catalytically active species can be encapsulated in the cavity; by limiting the moving space of the inclusions, the leaching and aggregation of catalytically active species can be suppressed during the reaction, leading to the excellent durability and reusability of the catalyst.[36,37] Secondly, adjustable pore structure and size of the carbon shell can regulate the mass transport and reaction characteristics, and further alter the catalytic selectivity.[38] Thirdly, the carbon shell provides a platform to anchor single atoms,[39,40] load metal particles,[41,42] and couple with multifunctional polymers,[43] which shows vast potential in variable catalysis applications. The rational design of nano-cavity or channel of HSC material can confine the metal nanoparticles (NPs) or cluster in a limited volume space, offering nanoconfinement effects to improve catalytic CO_2 reduction performance in terms of activity and selectivity. The positive influences of nanoconfinement mainly include (1) increasing

Hiromi Yamashita

Hiromi Yamashita has been a professor at Osaka University since 2004. He received a PhD degree from Kyoto University in 1987. He was an assistant professor at Tohoku University and an associate professor at Osaka Prefecture University. He has been the editor of Applied Catalysis B: Environmental since 2006, the president of the Asia-Pacific Association of Catalysis Societies (2019–2023), and the president of the Catalysis Society of Japan (2019–2020). His research interests include the design of single-site photocatalysts and nanostructured catalysts.

reactant molecule concentration in the confined space and enriching the surface overage of adsorbed species on the active sites,[44,45] (2) regulating the local pH value to hinder the competitive hydrogen evolution reaction during the eCO_2RR process,[46] and (3) tailoring the intrinsic electronic structures and optimizing the intermediate adsorption energy of the catalytic sites.[47] For instance, Zheng *et al.* reported that the confinement effect of N-doped carbon nanotubes (NCNT) enabled the attenuation of the binding strengths between Ni NPs and *CO intermediates; therefore, the NCNT-confined Ni NPs sample (Ni@NCNT) showed enhanced CO selectivity in eCO_2RR in comparison with the Ni NPs-supported sample (Ni-NCNT).[48] Pan *et al.* proposed that, in the hollow mesoporous carbon spheres (HMCS) confining Cu clusters electrocatalyst system, the nano-confinement effect of HMCS contributed to the facilitation of C–C bond coupling to produce C_2 products in eCO_2RR.[37] In our previous works, a series of novel hollow carbon nanocatalysts encapsulating alloys have been developed, which exhibit excellent thermocatalytic activity and stability for CO_2 hydrogenation to produce formate owing to the nano-confinement effects provided by the hollow carbon sphere.[49–51] Apart from CO_2 thermal conversion, our recent research demonstrated that HSC with superior conductivity and abundant pore structure can also serve as an effective support for syngas electrosynthesis from CO_2.[52] In our opinion, HSC-based catalysts are promising materials for CO_2 conversion, and they will continue to be hotspots in the thermocatalytic and electrocatalytic fields.

In the past few years, several valuable review articles related to the advancement and current status of hollow nanoreactors have been published. For instance, the review from Das *et al.* captured the advancements in catalytic CO_2 conversion, with a focus on novel core–shell catalyst development, activity, and selectivity improvement.[10] Kuang *et al.* reviewed the recent advances of metal@hollow carbon sphere catalysts in the fields of sustainable biomass and CO_2 conversion.[25] Li and co-workers reviewed the recent achievements of hollow carbon nanocages in the fields of energy storage and electrocatalysis.[53] Yu *et al.* reviewed the theoretical development of the hollow nanoreactor-based system, emphasizing the opportunities for the study of molecular kinetic behaviors in the hollow nanoreactors for achieving controllable catalysis.[54]

However, most of the reviews of HSC materials mainly focus on the energy storage field and biomass conversion, with a small amount concentrating on thermo- and electrocatalysis towards CO_2 conversion. Besides, a comprehensible summary of the structure–performance relationship of hollow carbon-based materials for CO_2 conversion remains to be refined. More importantly, the review content related to the popularly studied single-atom anchored on hollow carbon-based materials is relatively scarce. Considering the rapid development of studies on HSC-based catalysts in thermocatalytic and electrocatalytic CO_2 conversion, a timely cutting-edge review on this topic is of imperative need.

This review aims to offer a critical overview of the latest progress of HSC-based materials in thermocatalytic and electrocatalytic CO_2 conversion fields, with a discussion on the linkage of catalyst structure and activity (Fig. 1). The synthesis methods and functionalization strategies of HSC are also introduced. In the last section, an outlook for future research direction is proposed, targeting the current challenges.

2. Synthesis and functionalization of hollow-structured carbon materials

Generally, the HSC materials can be classified as hollow carbon spheres, hollow carbon nanotubes, hollow carbon polyhedrons, *etc.* motivated by the potentially utilitarian value for catalysis and energy storage, many efforts have been made toward the controllable synthesis and accurate design of hollow carbon with well-defined structures.[55–57] In this section, the synthetic methods and functionalization strategies are discussed.

2.1 Synthesis methods of HSC

2.1.1 Hard template synthesis. Hard template synthesis is by far the most commonly used way to prepare HSC.[58] As shown in Fig. 2a, a complete process of hard template technology involves four major steps: (1) preparation of the hard template, (2) coating template core with carbon shell precursors, (3) carbonization to obtain template@cabon under calcination treatment, and (4) template removal. The HSC synthesized by this method shows a highly regulated appearance, and the shape and size of its cavity can be tuned by choosing the suitable template material; usually, the morphology of the final product can be well predicted. Furthermore, the choice of carbon source determines the composition and physico-

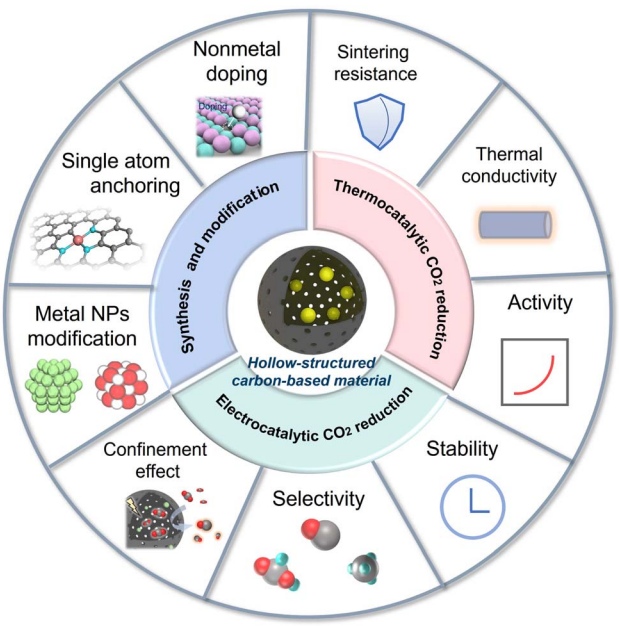

Fig. 1 Overview of the topics covered in this review. This review presents the syntheses, functionalization strategies of hollow-structured carbon (HSC) based materials, as well as their fascinating applications in electrocatalytic and thermocatalytic CO_2 conversion.

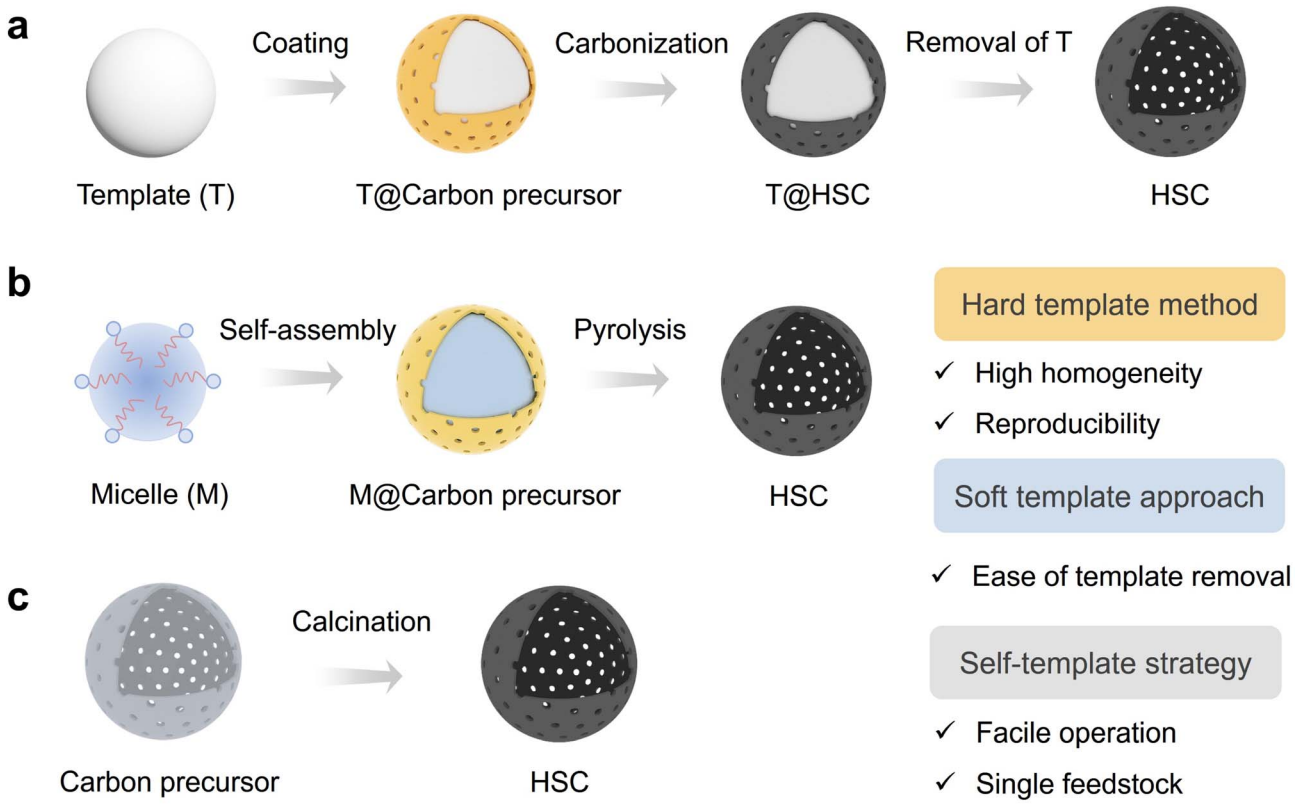

Fig. 2 Synthetic methods for hollow structured carbon (HSC). (a) Hard template method, (b) soft template approach, and (c) self-template strategy.

chemical properties of the carbon shell to some extent. A summary of recent representative works is presented in Table 1.

SiO_2 spheres are often used as hard templates to fabricate the HSC material due to the advantages of high stability, good uniformity, and ease of preparation. According to the study of Zhang *et al.*, mesoporous carbon hollow spheres (MCHS) were prepared using SiO_2 core particle and resorcinol–formaldehyde (RF) resin as a hard template and a carbon precursor, respectively (Fig. 3a).[59] As displayed in Fig. 3b and c, hollow cavity spaces were clearly seen in the spherical structure of MCHS.

Table 1 Parameter comparison of hard templating synthesis for HSC

Template	Carbon precursor	Template removal reagent	Hollow carbon type	Application	Ref.
SiO_2	Resorcinol and formaldehyde	HF	Mesoporous hollow carbon sphere	Supercapacitor	59
PMMA	Resorcinol and formaldehyde	Calcination	Hollow carbon sphere	Battery	64
PMMA	Dopamine	Calcination	Hollow carbon sphere	Electrocatalysis	65
SiO_2	Aniline	HF	Hollow carbon sphere	Supercapacitor	66
$CaCO_3$	Dopamine	HCl	Mesoporous hollow carbon sphere	Battery	67
SiO_2	Resorcinol and formaldehyde	NaOH	Mesoporous hollow carbon sphere	Microwave absorption	68
SiO_2	Dopamine	NaOH	Mesoporous hollow carbon sphere	Electrocatalysis	69
SiO_2	Resorcinol and formaldehyde	NaOH	Hollow carbon sphere	Thermal catalysis	51
CuO_2	3-Aminophenol and formaldehyde	HCl, H_2O_2	Hollow carbon sphere	Supercapacitor	70
Bi_2S_3	L-Cysteine and resorcinol	Calcination	Nanotube	Electrocatalysis	71
SiO_2	Resorcinol and formaldehyde	HF	Hollow carbon sphere	Supercapacitor	72
Urchin-like nickel	Urea	HCl	Urchin-like hollow carbon	Electrocatalysis	60
SiO_2	Pyrrole	HF	Hollow carbon sphere	Battery	73
SiO_2	Resorcinol and formaldehyde	HF	Hollow carbon sphere	Battery	74
SiO_2	Resorcinol, formaldehyde and melamine	KOH	Hollow carbon sphere	Electrocatalysis	75
SiO_2	Resorcinol and formaldehyde	HF	Hollow carbon sphere	Oil emulsification	76
SiO_2	Dopamine	NaOH	Hollow carbon sphere	Microwave absorption	77
SiO_2	Resorcinol and formaldehyde	NaOH	Hollow carbon sphere	Electrocatalysis	52

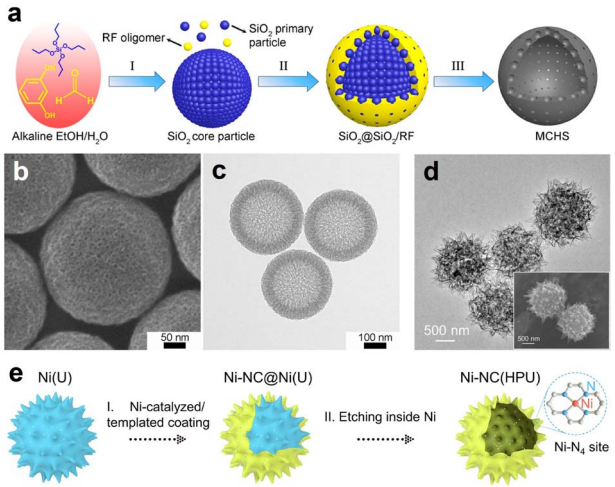

Fig. 3 (a) Schematic illustration of the synthesis procedure for mesoporous carbon hollow spheres (MCHS). (b) SEM and (c) TEM images of MCHS. Reproduced with permission from ref. 59. Copyright 2016, American Chemical Society. (d) TEM image, inset of (d) SEM image, and (e) preparation for single-Ni atoms anchored on hollow porous urchin-like N-doped carbon (Ni-NC(HPU)). Reproduced with permission from ref. 60. Copyright 2022, Wiley-VCH.

Notably, the pore size of carbon spheres can be manipulated by adjusting the synthesis conditions, such as the ratios of SiO_2 precursors (TEOS/TPOS) or solvents (ethanol/water). Taking the TEOS/TPOS ratio as an example, as the proportion of TPOS increases, the pore size of MCHS enlarges. In contrast to TEOS, the polymerization and condensation speeds of TPOS are slower. Consequently, larger silica aggregates are easily formed in the case of high-fraction TPOS, which contributes to the large mesopore formation in the following interaction process with RF oligomers. Therefore, the optimized preparation parameter is of great significance to obtain the desired HSC material. In addition to SiO_2, a metallic hard template is also available for the HSC preparation. Recent work from Li *et al.*, for instance, provided a strategy to prepare a N-doped urchin-like hollow carbon loaded with single-Ni atoms using solid urchin-like Ni and urea (providing C, N sources) as raw materials (Fig. 3d and e), where the Ni not only served as a hard template to assist the creation of hollow structure, but also offered the Ni source for the formation of Ni single sites.[60] Actually, the aforementioned method of integrating the metallic hard template with appropriate carbon sources may offer a new perspective for developing advanced nano-structured single-atom carbon-based catalysts.

2.1.2 Soft template method. Even though the hard template method offers numerous benefits, some drawbacks still exist. For example, the synthesis process of this approach is laborious; and the removal of the template involves the use of hazardous strong acids or bases. These issues stimulate the material researcher to exploit more facile and efficient syntheses of HSC. As illustrated in Fig. 2b, the soft templating method involves the utilization of thermally decomposable components (*e.g.*, micelles, emulsion droplets, or vesicles) as templates, wherein a carbon precursor is used to encapsulate these templates, obtaining a core–shell structured composite intermediate.[61,62] During the subsequent thermal treatment, the internal template decomposes while the external shell undergoes thermal fixation and carbonization. Eventually, a hollow carbonaceous material can be produced.

The soft templating approach for preparing HSC has gained considerable interest (Table 2), mainly due to the facile template fabrication and removal processes. In 2014, Wang *et al.* proposed a strategy to synthesize HSC using the mixed micelle converted from the P123 (EO_{20}–PO_{70}–EO_{20}) and sodium oleate as a soft template;[79] following this method, 2,4-dihydroxybenzoic acid and formaldehyde were served as carbon sources. Their results demonstrated that the diameter and shell thickness of HSC are highly related to the synthesis parameters, such as reaction temperature and the usage of polymer precursors.

The preparation of HSC with a single opening on the shell is an attractive method for increasing the diffusivity and accessibility of the guest species to the interior surface, while preserving the porous structure. Therefore, based on the traditional soft templating technique, Yu and co-workers developed a single-hole hollow carbon sphere through a poly(ethylene glycol) (PEG)-assisted emulsion-templating method, where PEG molecule functioned as a reverse demulsifier to manipulate the structure of HSC (Fig. 4a).[63] As revealed in Fig. 4b–d, hollow structured carbon spheres with a single hole can be observed, and the sizes of the hole and sphere are determined to be ~38 nm and ~138 nm, respectively. Additionally, by adjusting the molecular weight of PEG molecules, a closed-shell hollow carbon sphere, or bowl-like carbon can also be obtained. This work provides a new inspiration for the subtle preparation of HSC materials.

2.1.3 Self-template method. Different from the hard/soft template method, self-templating synthesis only involves the direct carbonization of the carbon-containing precursors to produce HSC (Fig. 2c). The emergence of the self-templated technique has reinvigorated the family of HSC synthetic approach (Table 2), which avoids the reliance on external templates and shows great potential for scalable fabrication.

Zhang *et al.* reported the fabrication of hollow carbon nanobubble with a shell thickness of only ~10 nm by simply calcining hollow ZIF-8 in a N_2 atmosphere (Fig. 5a).[85] It was proposed that, the distinctive hollow structured carbon featuring with ultra-thin shell not only serves to shorten the distance of ion diffusion distance but also provides a more accessible surface area for ions. Consequently, hollow carbon nanobubbles showed enhanced ion storage performance, as compared to the solid carbon nanoparticles. This synthesis concept is expected to stimulate the exploitation of more multifunctional hollow carbon materials derived from MOFs. In a separate study, Zheng *et al.* synthesized N, S co-doped hollow mesoporous carbon spheres (N/S-HMCS) using sulfur-bridged covalent triazine frameworks (S-CTF) sphere as a precursor (Fig. 5b).[89] The key point of this synthesis method is to control the pyrolysis temperature to regulate the polymerization degree of the inner and outer layers of S-CTF, which triggers the formation of the inner cavity. During the pyrolysis process, the

Table 2 Summary of the soft-templating and self-templating syntheses for HSC

Preparation method	Carbon precursor	Template	Morphology	Application	Ref.
Soft template	Glucose	Latex	Hollow carbon sphere	Battery	78
	2,4-Dihydroxybenzoic acid and formaldehyde	P123 and sodium oleate	Hollow carbon sphere	Hydrogenolysis of 5-hydroxymethylfurfural	79
	Ribose	Oleic acid emulsion	Flasklike hollow carbon	Supercapacitor	80
	Glucose	Oleic acid emulsion	Hollow carbon sphere	Biochemistry and supercapacitor	81
	Aniline and pyrrole	F127	Hollow carbon sphere	Sodium storage devices	82
	2,4-Dihydroxybenzoic acid and hexamethylenetetramine	P123 and sodium oleate	Single-hole hollow carbon sphere	Liquid-phase adsorption	63
Self-template	Melamine and formaldehyde resin	—	Hollow carbon microsphere	Supercapacitor	83
	Poly(amic acid)	—	Hollow carbon microsphere	Supercapacitor	84
	Monocrystalline zeolitic imidazolate framework (ZIF-8) nanobubble	—	Hollow carbon nanobubble	Battery	85
	Deep eutectic solvent (urea, 2,5-dihydroxy-1,4-benzoquinone and $ZnCl_2$)	—	Hollow carbon nanorod	Supercapacitor	86
	Poly(hexachlorocyclotriphosphazene-tannic acid-4,4′-sulfonyldiphenol) hollow nanosphere	—	Hollow carbon sphere	Electrocatalysis	87
	Polydopamine vesicle	—	Hollow carbon cage	Cathode for Li–S batteries	88
	Sulfur bridge covalent triazine framework sphere	—	S, N-doped hollow carbon sphere	Electrocatalysis	89
	Tetrahydrofuran-treated resorcinol-formaldehyde (RF) polymer sphere	—	Concave hollow carbon sphere	Anode material for Na/K-ion battery	90

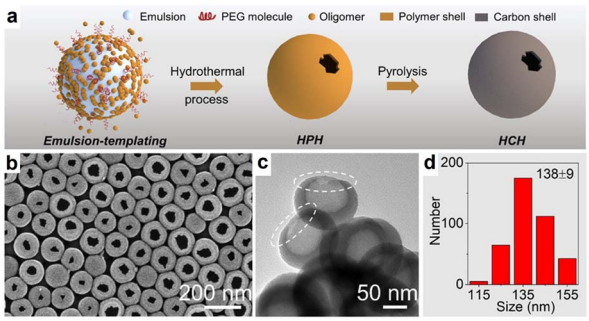

Fig. 4 (a) Schematic diagram of the synthesis for single-hole hollow carbon spheres (HCH). (b) SEM and (c) TEM images, and (d) diameter distribution of HCH. Reproduced with permission from ref. 63. Copyright 2022, American Chemical Society.

volatile substance generated from the thermal decomposition of the central oligomer with a lower polymerization degree gradually migrated to the outside to reduce the surface energy and maintain the structural stability. With the temperature increase from 500 °C to 900 °C, the internal cavity size gradually became larger and the specific surface area increased from 12 $m^2\ g^{-1}$ (N/S-HMCS500) to 331 $m^2\ g^{-1}$ (N/S-HMCS900). This study proposes a promising route toward the controllable synthesis of hollow carbon material with tailored heteroatom doping.

In general, the selection of an appropriate synthesis method for HSC should meet the demand of the intended application scenario. The hard template method is more recommended for applications requiring high product homogeneity and experimental reproducibility. Nevertheless, this approach still has some limitations, including the complex and time-consuming procedures and the use of corrosive reagents for template removal. In contrast, the soft template method offers a relatively easy template removal process; however, challenges arise concerning the maintenance of structure rigidity throughout

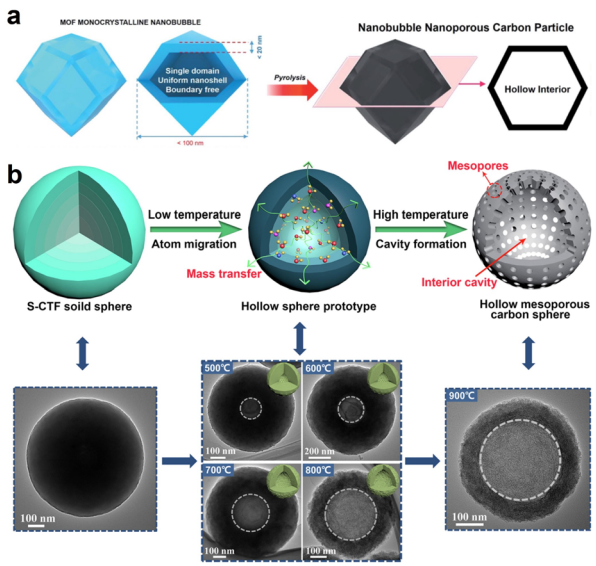

Fig. 5 (a) Preparation of nanobubble carbon *via* the pyrolysis of MOF nanobubbles. Reproduced with permission from ref. 85. Copyright 2017, Royal Society of Chemistry. (b) The fabrication process of N, S co-doped hollow mesoporous carbon sphere (N/S-HMCS) and the corresponding TEM images. S-CTF represents the sulfur-bridged covalent triazine frameworks. Reproduced with permission from ref. 89. Copyright 2021, Elsevier.

subsequent applications. Although the template method shows some advantages in the aspect of controlling the particle size uniformity and dispersion of HSC, the self-templated method is still regarded as a promising route for achieving scalable production due to its facile operation and utilization of only a single feedstock.

2.2 Functionalization strategies

2.2.1 Nonmetal doping. External nonmetal heteroatoms (nitrogen (N), phosphorus (P), sulfur (S), fluorine (F), *etc.*) doping, which has long been well-established in the study of carbon materials, provides a feasible modification route to regulate the charge redistribution, CO_2 affinity, and electrical conductivity.[91–94] Thus far, the most well-established strategy is the introduction of N with high electronegativity (3.04) into the carbon framework (carbon electronegativity: 2.55), and it can change the asymmetric electron spin density and improve the intrinsic activity.[95–97] For example, Wu *et al.* synthesized a high-efficiency nitrogen-doped carbon nanotube catalyst (NCNT) with the aid of a liquid chemical vapor deposition (CVD) method.[98] It was found that the electrochemical CO_2-to-CO conversion performance of NCNT even surpassed those of noble metals (Au and Ag), achieving a similar CO selectivity at a lower overpotential. In sharp contrast to NCNT, the pristine CNT exhibited poor activity and selectivity. As evidenced by the experimental characterization and DFT theoretical calculations, the features induced by N doping, including high conductivity, efficient catalytic sites, and a low energy barrier for CO_2 activation, benefits CO_2 electroreduction process. In another example, Wang *et al.* integrated NCNT and N-doped porous carbon to a composite membrane, and it was demonstrated to serve as an efficient metal-free catalyst for electrochemical CO_2 reduction to produce formate;[99] the results highlighted the advantage of the nitrogen doping effect in the improvement of electrochemical stability and anti-oxidizability.

In addition to N, F doping is identified as an efficient way to tailor the electronic structure of carbon catalysts and enhance eCO_2RR activity by forming a local positive charge area, and the local positive charge area can elevate COOH* (an important intermediate) adsorption and suppress the side-competing hydrogen evolution reaction (HER).[100,101] To further increase the surface area, Ni *et al.* developed a F-doped cagelike carbon electrocatalyst, which exhibits excellent CO product selectivity at high overpotential.[102] The results demonstrated that hollow morphology with abundant mesopores and micropores can facilitate the capture and diffusion of CO_2 molecules. Additionally, a strong electric field formed at the edge site of the opening pores on the F-doped carbon shell can increase the partial concentration of electrolyte cations (K^+), thus lowering the eCO_2RR thermodynamic energy barrier and boosting the activation of CO_2.

Besides single-element doping, multiple-element doping has recently been proven to be effective in synergistically improving the eCO_2RR performance of HSC materials. Li *et al.* developed a N, S dual co-doped hollow carbon sphere, which showed a high CO faradaic efficiency (FE_{CO}) of 93% at a low potential of −0.6 V (*vs.* RHE), surpassing that of single-N-doped counterpart.[103] The addition of S doping provided more active sites, and decreased the Gibbs free energy for the formation of COOH* intermediate, thus promoting the eCO_2RR activity. Furthermore, N, B co-doped hollow carbon spheres reported by Cheng *et al.* also exhibited a high FE_{CO} of 95.1% at a low overpotential of 310 mV.[104] It was suggested that doped B sites enhance CO_2 adsorption, while N sites promote the hydrogenation of $*CO_2$ to form COOH*.

Although encouraging progress has been made in developing non-metal-doped carbon materials, some issues still need to be solved. Taking N-doping carbon as an example. The identification of actual active sites in N-doped carbon catalyst is still controversial;[105] because, during the doping process, different kinds of nitrogen configurations, including pyridinic-N, pyrrolic-N, and graphitic-N, will be introduced to the carbon framework, resulting in structural inhomogeneity.[106] It is difficult to precisely control the N configuration. Furthermore, interactions between different types of nitrogen potentially exist, which may affect the CO_2 catalytic reaction process.[96] The combination of advanced *in situ* characterization techniques and DFT simulation is needed to further clarify the structure–activity relationship and understand the relevant reaction mechanism.

2.2.2 Metal single-atom anchoring. Since the emergence of single-atom catalysts (SACs) concept in 2010, SAC has received interdisciplinary attention and become the frontier hotspot in catalysis field due to its exceptional catalytic properties.[107] The atomic scale metal sites endow the catalyst with many attractive advantages in catalytic CO_2 reduction: (1) high atom utilization efficiency allows to lower the cost, especially in the case of noble metal.[108,109] (2) Excellent activity and selectivity can be achieved by regulating the single atom coordination environment and electronic structure.[110,111] (3) Well-defined active sites provide ease for the catalytic mechanism study.[112]

Normally, the isolated metal atoms with high surface energy are unstable and easy to migrate and coalesce.[113] Integrating single-atom active sites with the aforementioned heteroatoms-doping HSC material prevents the aggregation of single atoms and endows HSC considerable catalytic activity simultaneously. For example, Pan *et al.* developed a highly dispersed $Co–N_5$ site anchored on a hollow carbon sphere (Fig. 6a and b), and it showed high-efficiency CO_2 electroreduction reactivity with FE_{CO} reaching 99.2% and 99.4% at −0.73 and −0.79 V *vs.* RHE, respectively (Fig. 6c).[114] In contrast, cobalt phthalocyanine (CoPc, Co–N coordination number is 4) showed relatively low FE_{CO}, implying the positive roles of $Co–N_5$ sites. As verified by the DFT calculation results (Fig. 6d), the excellent eCO_2RR activity is associated with the existence of single-atom $Co–N_5$ sites and the resulting enhanced CO_2 activation, rapid formation of COOH*, and improved CO desorption. Similarly, by loading single-atom $Ni–N_x$ sites on the well-regulated carbon structure of HSC-based catalysts, desired electrochemical eCO_2RR performance can be achieved.[115–117] Furthermore, atomically dispersed Ru(III) supported on a N-doped carbon sphere also showed satisfactory activity and stability in continuous CO_2 hydrogenation test, owing to the strong

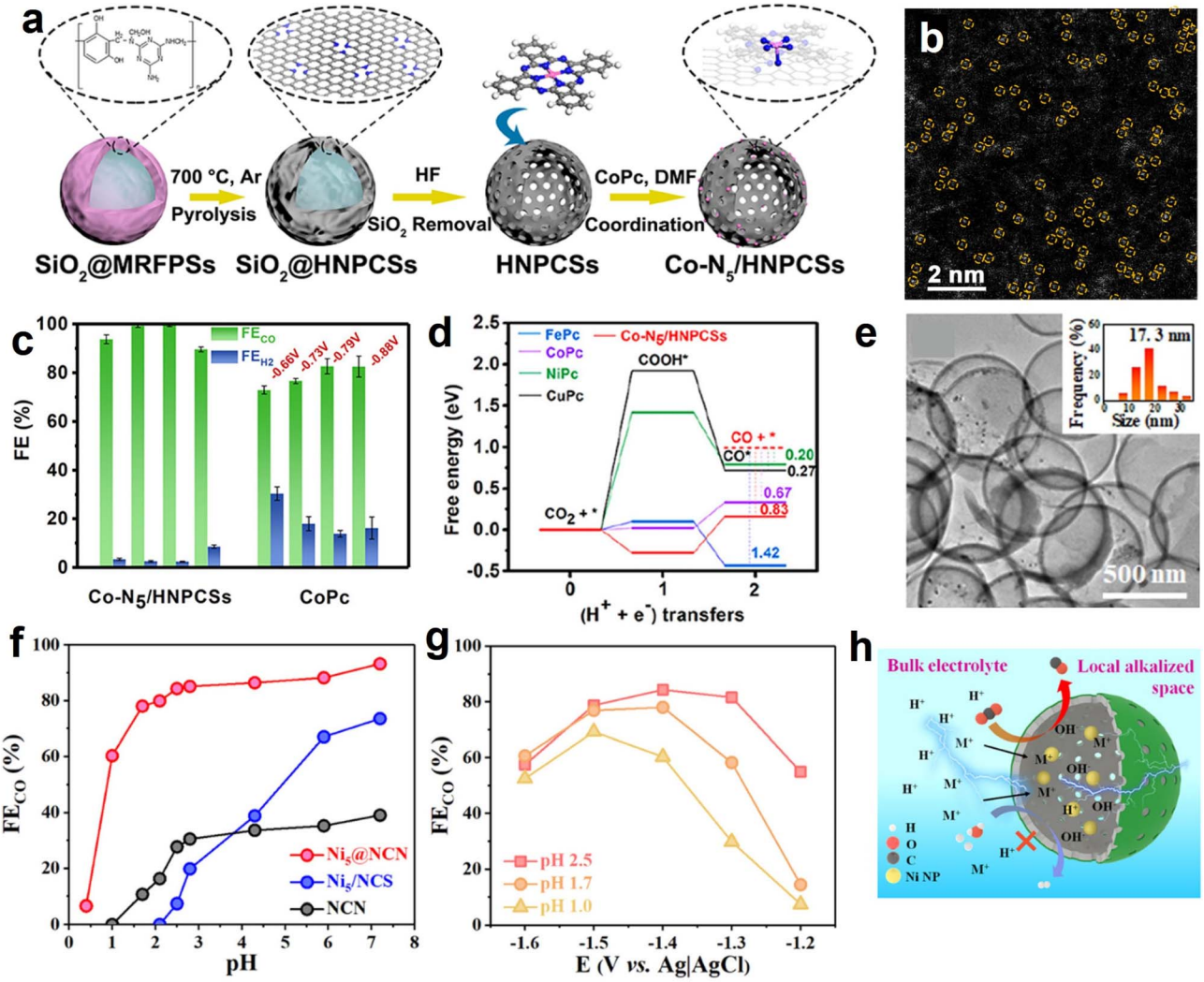

Fig. 6 (a) Synthesis procedures and (b) magnified HAADF-STEM image of hollow N-doped porous carbon spheres with single-atom Co–N_5 sites (Co-N_5/HNPCSs). (c) Faradaic efficiencies for CO and H_2 production at the given potentials over Co-N_5/HNPCSs and CoPc. (d) Calculated eCO_2RR free energy profiles of Co-N_5/HNPCSs catalyst and MPc (M = Co, Fe, Ni, Cu). Reproduced with permission from ref. 114. Copyright 2018, American Chemical Society. (e) TEM image of Ni NPs@N-doped carbon nanocages (Ni@NCN). The inset shows the metal NPs size distribution. (f) FE_{CO} and (g) current density of the best-performing Ni@NCN sample in acidic electrolyte condition. (h) Schematic diagram of the pH environment and ions transportation around the Ni@NCN catalyst. Reproduced with permission from ref. 46. Copyright 2022, American Chemical Society.

binding strength between Ru(III) species and pyridinic N/pyrrolic N site.[118]

As mentioned above, single-atom modification plays a significant role in improving the eCO_2RR performance of HSC-based materials. However, some important aspects still need to be further investigated: (1) the coordination environment has great impact on the electronic structure of SACs, so unveiling the relationship between the coordination number or connecting heteroatom type of SACs and eCO_2RR activity is important; (2) at present, most of the SACs syntheses are still at the laboratory stage; a universal approach for large-scale SACs production is required to meet the demands of practical applications;[119] (3) some studies suggest that single-atom site configuration only shows high reactivity in the primary reaction process and is inadequate for the subsequent catalytic reaction steps involving multiple electron transfer and intermediate conversion, accordingly, developing novel catalysts with dual atomic sites may overcome this limitation.[120,121]

2.2.3 Metal nanoparticles modification. Metal nanoparticles (NPs) modified HSC material as active and reusable catalysts have attracted wide interest in the field of catalytic CO_2 reduction, in which metal NPs act as the active sites. The catalytic activity and selectivity can be tuned by the adjustment of their morphology,[122] crystal facet,[123] and composition,[124] *etc.* For HSC supports, they can provide a unique space-confined structure to stabilize metal NPs; and they serve to prevent the agglomeration and leaching of the metal NPs, while allowing the diffusion of the reactant molecules to the active sites (metal NPs).

In view of the fact that HCS coupling with metal NPs can build a high-efficiency nanoreactor, Liu *et al.* designed a hollow

N-doped carbon nanocage catalyst with Ni nanoparticles being encapsulated within the cavity (Ni@NCN) (Fig. 6e).[46] Benefiting from nanoconfinement, the optimized sample (Ni_5@NCS) showed excellent eCO_2RR activity, achieving a high FE_{CO} of 93.2% in neutral media. Furthermore, Ni_5@NCS likewise exhibited decent performance in acid conditions, markedly exceeding the control samples of non-hollow-structured Ni/N-doped carbon sphere (Ni-NCS) and Ni-free N-doped carbon nanocage (NCN) (Fig. 6f). It is noteworthy that the FE_{CO} of Ni_5@NCS can achieve 84.3% even in the electrolyte of pH 2.5 at −1.4 V *vs.* Ag/AgCl (Fig. 6g). The superior activity is ascribed to the local pH-regulator effects of hollow carbon nanoreactor by concentrating the OH^- ions within the cavity (Fig. 6h). Specifically, the consumption rate of the H^+ in the hollow carbon nanocage is faster than the replenishment rate of H^+ because of the proton transport limitation, leading to a local alkaline environment and suppressing the competing hydrogen evolution reaction (HER). Recently, the effectiveness of metal NPs and HSC composite in electrochemical CO_2 reduction for CO production has also been demonstrated on the Ni NPs@N-doped nanotube systems.[125,126] Previous studies have shown that alloy NPs show superior performance over monometallic NPs in CO_2 activation and formate formation.[36,127] Motivated by this, our group developed a PdCu alloy NPs confined within hollow carbon sphere catalyst (PdCu-N@HCS) (Fig. 7a and b), which showed an excellent thermal-catalytic CO_2 hydrogenation activity, delivering the highest turnover number hydrogenation activity, delivering the highest turnover number (TON) of 1432 at 100 °C for 24 h compared to single-metal-component samples (Fig. 7c);[49] DFT calculation result demonstrated that the alloying of Pd with Cu effectively reduces the energy barrier of the H_2 dissociation, and is capable of facilitating the HCO_3^- transformation.

In conclusion, metal NPs coupled with HSC showed satisfactory catalytic activity in some electrocatalysis and thermal catalysis applications. However, the activity improvement may still profit from the consideration of the following aspects. Incorporating HSC with novel high-entropy alloys (HEAs), a new class of multi-component alloys that possess numerous advantages (*e.g.*, flexible component adjustability, high oxidation resistance and excellent corrosion resistance), is expected to design high-efficiency catalysts. Recently,

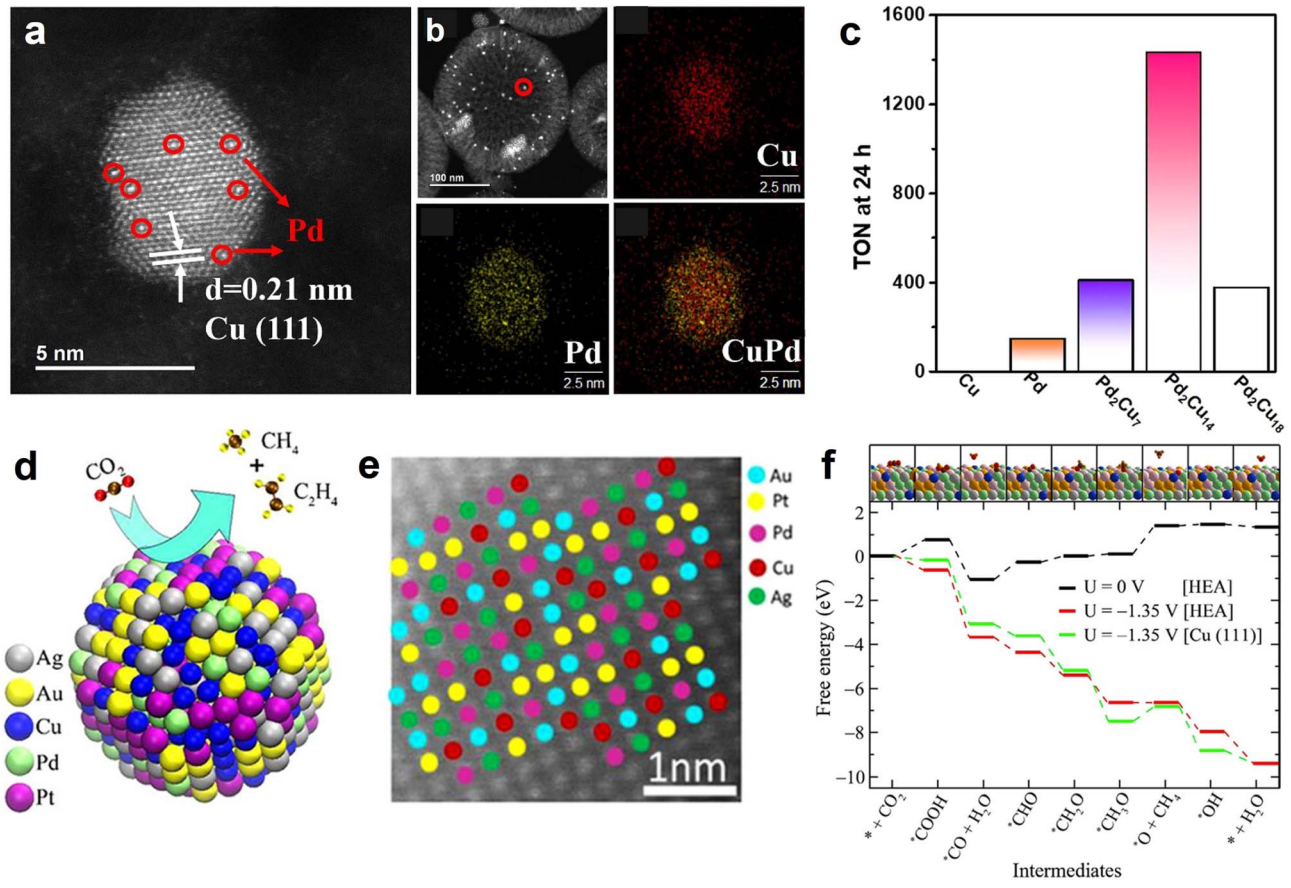

Fig. 7 (a) Magnified HAADF-STEM image of CuPd alloy NPs and (b) STEM image and the corresponding EDS elemental maps of Cu, Pd and CuPd of PdCu-N@MHCS sample. (c) Effect of the Pd/Cu molar ratio on Pd_xCu_y-N@MHCS for the hydrogenation of CO_2 to formate. Reproduced with permission from ref. 49. Copyright 2021, American Chemical Society. (d) Illustration of electrochemical CO_2 conversion and (e) HR-STEM image of HEA alloy NPs (AuAgPtPdCu). (f) Comparision of eCO_2RR free energy on AuAgPtPdCu HEA and Cu (111). The Pt, Pd, Ag, Au, Cu, C, O, and H atoms are shown in gray, green, pink, yellow, blue, brown, red, and orange, respectively. Reproduced with permission from ref. 128. Copyright 2020, American Chemical Society.

Nellaiappan *et al.*, delicately fabricated a HEA catalyst (AuAgPtPdCu) (Fig. 7d and e), which can be used for efficient electrochemical CO_2 conversion, with the FE of 67.5% for gaseous hydrocarbons (CH_4, C_2H_4) at −0.3 V *vs.* RHE;[128] the free energy diagram of eCO_2RR results showed that, at a given potential of −1.35 V, the reaction profiles of HEA and Cu (111) are downhill in general. Notably, at the $*OCH_3$ to *O transition step, the energy barrier on Cu (111) surface is obviously larger than that of HEA (Fig. 7f), suggesting that the thermodynamic favorability of eCO_2RR on the HEA system is higher than on pristine Cu. This work demonstrates that HEA can effectively alter the reaction energy barrier of the intermediates, and accelerate the CO_2 multi-electron reduction process. In another study, Pedersen *et al.* corroborated the feasibility that HEA material with optimized components and content can be employed as an efficient eCO_2RR catalyst, by using DFT calculation and machine learning.[129] In addition, the introduction of aminopolymers into metal NPs@HSC catalyst system is also worth studying, because aminopolymers contain plenty of amine groups with basicity that can promote CO_2 capture ability.[130] Another merit of aminopolymer is the anchoring of metal ions prior to the metal nucleation, thus facilitating the dispersion of metal NPs.[131] Our previous works have proved the positive effects of aminopolymer in the nanoconfined reactor for CO_2 electroreduction and thermo-catalytic conversion.[52,132] The above-mentioned directions may provide more possibilities for designing high-performance metal NPs@HSC-based catalysts.

3. Electrocatalytic CO_2 conversion of hollow carbon-based materials

Electrochemical CO_2 conversion to produce fuels and chemicals is considered as an ideal option for responding to the increasing energy supply requirement and environmental concerns.[135,136] Typically, a CO_2 electroreduction cell comprises two electrodes: cathode (for eCO_2RR) and anode (for water oxidation). By applying an external bias, the eCO_2RR occurs at the three-phase interface of the cathode, electrolyte, and the adsorbed CO_2, with value-added products (CO, $HCOO^-$, C_2H_4, *etc.*) being obtained. The commonly used reactors for eCO_2RR can be categorized into three types: (1) H-type cell (Fig. 8a), (2) liquid-flow cell (Fig. 8b), and (3) membrane electrode assembly (MEA) cell (Fig. 8c). The H-type cell involves the use of aqueous electrolytes, wherein the solubility of CO_2 is relatively low (approximately 34 mM). Therefore, CO_2 electrolysis on the H-type cell is susceptible to the influence of mass transport limitations, leading to low current densities (<100 mA cm^{-2}).[110,133] In the liquid-flow cell, an ion exchange membrane is used to separate the cathode and anode to prevent the CO_2 reduction products in the cathode from transferring to the anode and undergoing re-oxidation. Additionally, the anolyte and catholyte are continuously cycled. Different from the H-type cell, eCO_2RR occurs at the gas diffusion electrode (GDE), overcoming the solubility and mass transport limitations of CO_2 in aqueous electrolytes and enabling a high current density to be achieved (>100 mA cm^{-2}).[134] In contrast to H-cell and liquid-flow cells,

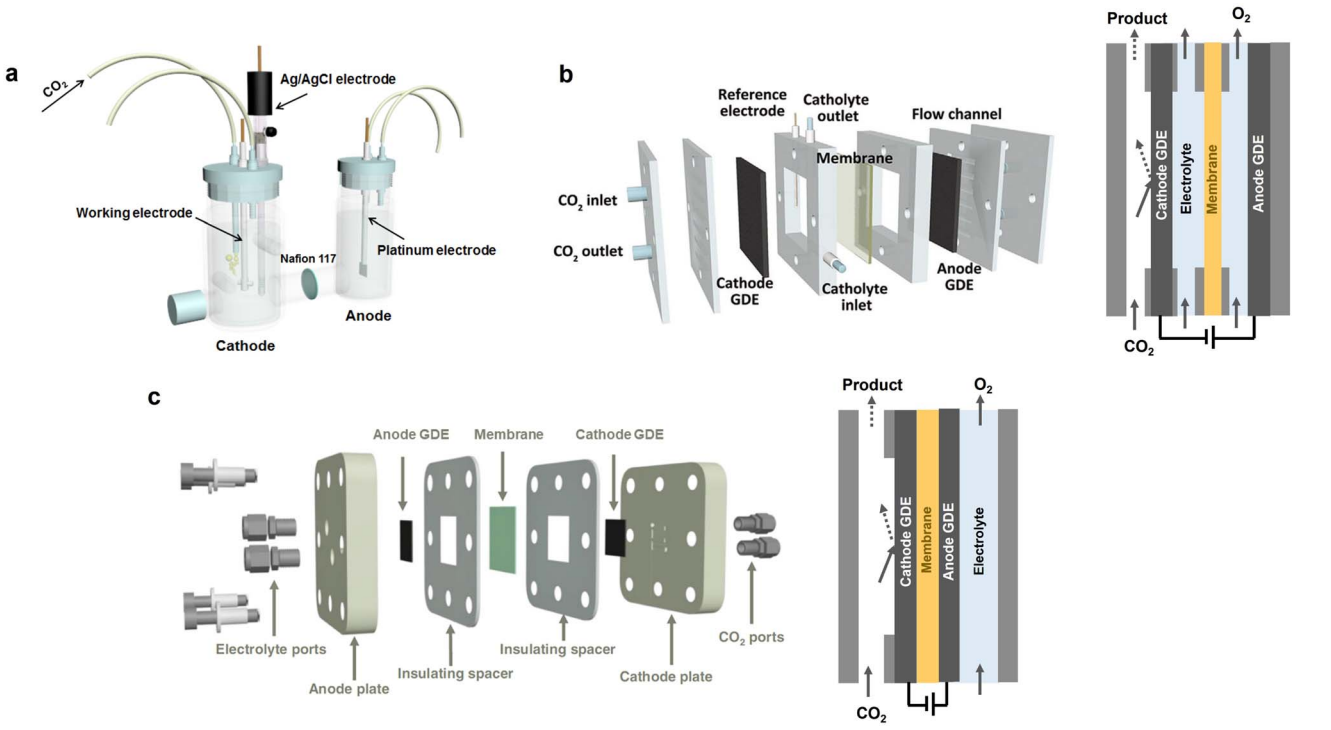

Fig. 8 Schematic illustrations of the eCO_2RR reactors. (a) H-cell. Reproduced with permission from ref. 133. Copyright 2018, Elsevier. (b) Liquid-flow cell. Reproduced with permission from ref. 134. Copyright 2021, Wiley-VCH. (c) MEA cell. Reproduced with permission from ref. 110. Copyright 2023, Springer Nature.

Table 3 Performance comparison of HSC-based catalysts for electrochemical CO_2 conversion

Catalyst	Faradaic efficiency (%)	Partial current density (mA cm^{-2})	Potential (V *vs.* RHE)	Electrolyte	Reactor type	Ref.
Co-N_5/HNPCSs	CO, 99.4	~4.5	−0.73	0.2 M $NaHCO_3$	H-type cell	114
Ni/N-doped carbon sphere	CO, ~80	~4	−0.78	0.5 M $KHCO_3$	H-type cell	116
F-doped cagelike carbon	CO, 88.3	~32	−1.0	0.5 M $KHCO_3$	H-type cell	102
Ni SAs/N-doped carbon sphere	CO, 95.1	~7.6	−0.8	0.5 M $KHCO_3$	H-type cell	155
Ni-N_4/carbon sphere	CO, 95%	10.5	−1.0	0.5 M $KHCO_3$	H-type cell	115
Ni/N-HCS	CO, 97%	10	−0.8	0.5 M $KHCO_3$	H-type cell	117
N, B co-doped HCS	CO, 95.1	~1	−0.42	1.0 M $KHCO_3$	H-type cell	104
Ni/N doped hollow carbon plates	CO, ~100	18.2	−1.0	0.5 M $KHCO_3$	H-type cell	156
Ni-N_3/NHCSs	CO, 98.57	~14.2	−0.87	0.5 M $KHCO_3$	H-type cell	146
Ni NPs/N doped carbon cage	CO, 93.2	17.1	−0.8	0.5 M $KHCO_3$	H-type cell	46
Ni-N doped HCS-Micro/Meso	CO, 98.3	16.2	−1.0	0.5 M $KHCO_3$	H-type cell	38
Ni SAs/N-doped urchin-like carbon	CO, 91	24.7	−0.8	0.5 M $KHCO_3$	H-type cell	60
Hollow carbon with CoN_4O and ZnN_4 dual atomic sites	CO, 92.6	15.57	−1.0	0.5 M $KHCO_3$	H-type cell	157
Ni SAs/N-doped carbon sphere	CO, 94.91	15.35	−0.8	0.5 M $NaHCO_3$	H-type cell	147
	CO, 98.41	100	—	1 M $KHCO_3$	Flow cell	
SnO_2/carbon sphere	Formate, 54.2 CO, 21.8	Formate, 3.7 CO, 1.4	−0.9	0.1 M $KHCO_3$	H-type cell	158
Bi NRs@NCNT	Formate, 90.9	5.9	−0.9	0.1 M $KHCO_3$	H-type cell	71
Cu/HCS	Formate, 82.4	26	−0.81	0.5 M $KHCO_3$	H-type cell	41
SnS_{2-x}/NHCS	Formate, >80	~30	−1.2	0.5 M $KHCO_3$	H-type cell	159
Cu cluster/HMCS	C_{2+} products (C_2H_5OH and C_2H_4), 88.7	~240	−1.0	1.0 M KOH	Flow cell	37
Cu_2O/NCNT	C_{2+} products (C_2H_5OH and C_2H_4), 77.61	16.79	−1.1	0.1 M $KHCO_3$	H-type cell	160

the anode and cathode in MEA cell are directly compressed with the ion exchange membrane, forming a sandwich structure (Fig. 8c). This zero-gap structure significantly reduces the distance between the anode and cathode, thus minimizing ohmic resistance and markedly enhancing energy efficiency and stability.[137] Generally, the H-type cell is suitable for the fundamental study of eCO_2RR as well as the screening of efficient catalysts, due to the ease of operation and the rapid testing. Among the above-mentioned eCO_2RR cells, the MEA cell holds the most promising industrial potential for eCO_2RR, as it shows better energy utilization efficiency and stability. The development of more high-performance membranes will benefit the further improvement of the efficiency for MEA cells.

The choice of electrolytes is important to increase the activity and selectivity of electrochemical CO_2 reduction.[138,139] Taking the widely used alkali metal bicarbonate electrolytes as examples, the size of alkali metal cation is able to affect the hydrolysis constants of hydrated cations, thereby altering the local pH value and CO_2 concentration around the electrode; eventually, it will cause a change of the selectivity toward C_1 products on Ag and C_2 products on Cu.[140] Additionally, the selectivity of eCO_2RR is also associated with the concentration of cations. For instance, Marcandalli *et al.* reported that at low potentials (>−0.4 V *vs.* SHE), a high concentration of Na^+ cations is beneficial for enhancing the FE_{CO}, contrasting with the situation at more negative potentials (<−0.4 V *vs.* SHE), where a low concentration of Na^+ cations is more favorable for suppressing hydrogen evolution and improving the FE_{CO}.[141] In general, the electrolyte type can serve as a crucial design parameter, enabling the tailoring of the electrocatalyst–electrolyte interfacial environment to obtain desired products in the reduction of CO_2.

eCO_2RR involving multiple proton-coupled electron transfer processes usually requires overcoming high thermodynamic and kinetic barriers.[142,143] The development of reliable electrocatalysts is of great significance to regulate the charge transfer and reaction intermediate adsorption/activation, overcoming the aforementioned obstacles, and achieving high catalytic activity and selectivity. As a result of recent research efforts, a series of high-performance HSC-based electrocatalysts have emerged (Table 3), which have creatively exploited the structural advantages of HSC, broadening the understanding of the mechanism behind eCO_2RR. In this section, the discussion mainly focuses on product selectivity with the aim of providing insights into the structure–activity relationships of HSC-based materials.

3.1 Selective production of CO or syngas (CO and H_2)

Atomically dispersed metal–nitrogen sites (M–N_x) modified carbon materials are widely studied in electrocatalysis, especially electrocatalytic CO_2 reduction, due to the well-tuned electronic characteristic and appropriate binding strength for the reaction intermediate. The merits of abundantly accessible sites, unique cavity space, and good permeability enable HSC materials to be appealing supports for anchoring the atomically dispersed M–N_x sites.

Notably, a majority of the recent studies focus on HSC-based catalysts with Ni–N_x sites and their electrochemical CO_2-to-CO conversion applications (Table 3). Herein, we use this type of material as the main line to introduce their CO_2-to-CO applications. To begin with, Xiong *et al.* developed a single-atom hollow carbon sphere catalyst containing Ni–N_4 atomic sites for eCO_2RR to CO.[115] The best-performing sample (Ni-HMCS-3-800) delivered an extremely high turnover frequency value of 15 608 h^{-1}, and the FE_{CO} above 95% at a wide potential range (−0.7 to −1.1 V *vs.* RHE) (Fig. 9a and b). It was demonstrated that the remarkable activity originated from the improved CO_2 adsorption and activation capacity, which are associated with the optimization of the geometrical structures of carbon support, including the shell thickness and compactness. Besides, this work also highlighted the importance of pore structure in eCO_2RR; the appropriate mesopore size distribution (∼7–10 nm) endows Ni-HMCS-3-800 with enhanced diffusion and overflow of the reactants. As a result, Ni-HMCS-3-800 showed higher catalytic activity in comparison to the Ni-HMCS-3-700 sample with a smaller mesopore size (∼3.1 nm).

Recently, the effects of the coordination environment of the central metal Ni–N_x on eCO_2RR activity have received considerable attention.[144] As documented in the literature, the energy barrier for *COOH intermediate formation on the Ni–N_3 site is lower than that of the Ni–N_4 site, suggesting coordinatively unsaturated Ni–N_3 may be favorable for eCO_2RR.[145] Accordingly, Gong *et al.* synthesized Ni–N_3 units embedded in nitrogen-doped hollow carbon spheres (Ni-NC/NHCSs) by a hard template method using NiPc (Ni source) and dopamine (carbon and nitrogen sources) as precursors (Fig. 9c).[146] The optimized catalyst (Ni-NC/NHCSs-600) exhibited a maximal FE_{CO} of 98.57% at −0.87 V *vs.* RHE, which is significantly larger than the value of its counterpart NiPc@NHCSs (FE_{CO} = 19.61%). Additionally, in sharp contrast to NiPc@NHCSs (stability < 2000 s), Ni-NC/NHCSs-600 showed a long-term stability of 14 h with a negligible current attenuation. In a separate study, the researchers of the same group rationally developed a novel catalyst consisting of Ni-C_3N_1 moiety confined in hollow carbon reactors (I-Ni SA/NHCRs), which was reported to achieve a high FE_{CO} of 94.91% at −0.80 V in H-cell, and showing higher CO partial current density (−15.35 mA cm^{-2}) than that with outer Ni-C_2N_2 moiety (O–Ni SA/NHCRs, −12.06 mA cm^{-2}), or without hollow structure (Ni-NC, −5.39 mA cm^{-2}).[147] More importantly, a high FE_{CO} of up to 98.41% was achieved for I-Ni SA/NHCRs at 100 mA cm^{-2} in a flow cell with 1 M $KHCO_3$ electrolyte, implying a huge potential for practical application. It was proposed, based on COMSOL multiphysics finite element simulations, that the diffusion time of CO_2 molecules in hollow nano-reactor structure (model II, I-Ni SA/NHCRs-based electrode) (CO_2 diffusion time, ∼1.25 s) is much faster than that of solid sphere structure (model I, Ni-NC-based electrode) (CO_2 diffusion time, >2.0 s) (Fig. 9d), as a result of the intrinsically structural virtue; in the meantime, the bottom and average concentration of CO_2 in the above two models was dynamically monitored *via* the simulation probe (Fig. 9e and f), and the results fully confirmed the facilitated CO_2 diffusion rate in hollow structural carbon. Obviously, it is conducive to the accessibility of isolated Ni

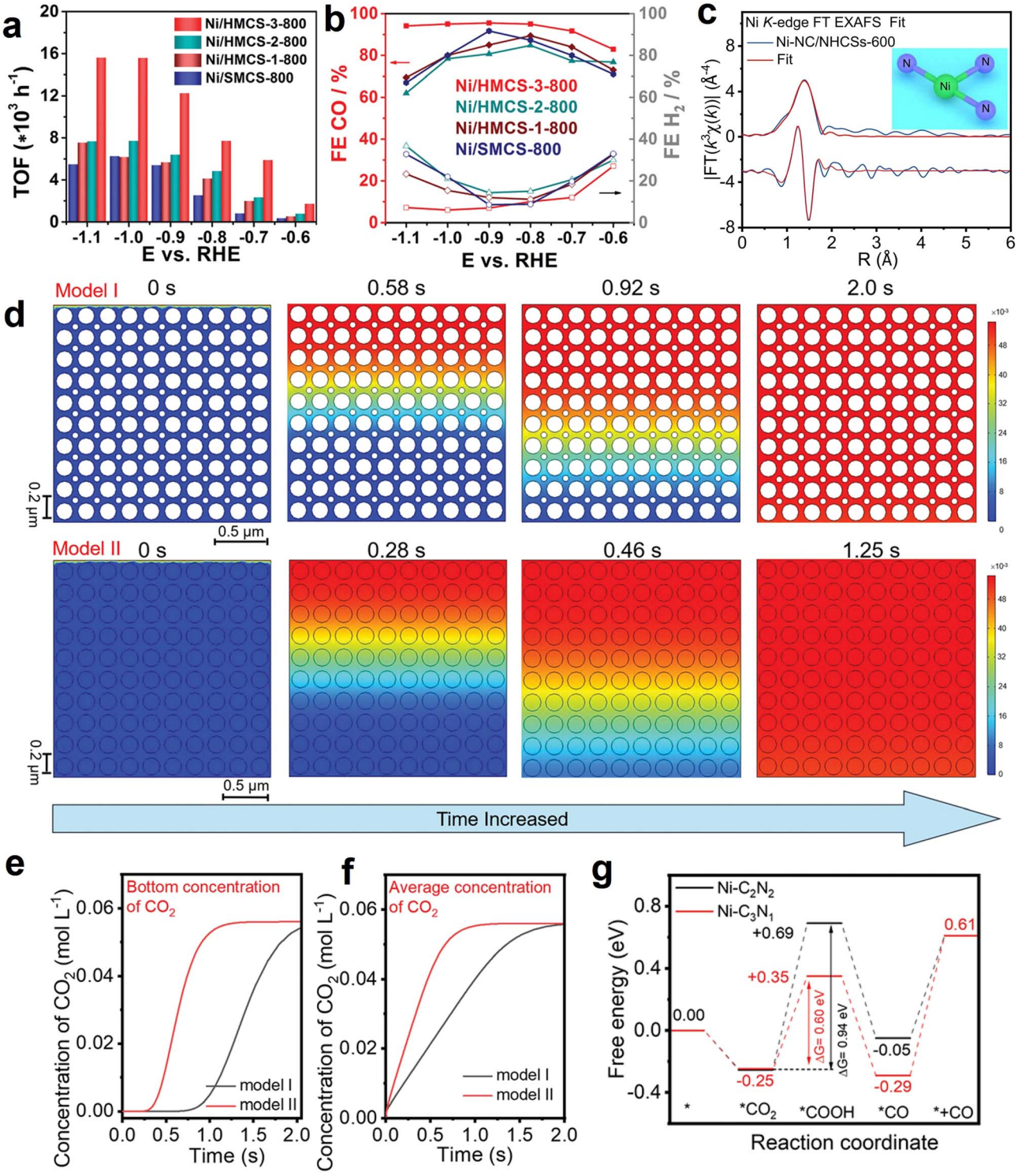

Fig. 9 (a) Turnover frequency (TOF) and (b) faradaic efficiencies of CO and H_2 of as-synthesized samples at given potentials. Reproduced with permission from ref. 115. Copyright 2020, Wiley-VCH. (c) Ni K-edge fitting curve of Ni-NC/NHCSs-600 in *R* space. The upper and lower traces represent the magnitude and imaginary part, respectively. The inset shows the model of Ni-N_3 moiety. Reproduced with permission from ref. 146. Copyright 2022, Elsevier. (d) COMSOL multiphysics finite element simulation results of CO_2 diffusion time in 0.5 M $NaHCO_3$ aqueous solution for solid sphere structure (model I, Ni-NC-based electrode) and hollow nano-reactor structure (model II, I-Ni SA/NHCRs-based electrode). (e) Bottom and (f) average concentration of CO_2 for model I and model II *via* probe monitoring. (g) Calculated eCO_2RR free energy profiles of Ni-C_3N_1 and Ni-C_2N_2 moiety. Reproduced with permission from ref. 147. Copyright 2023, Wiley-VCH.

active sites in I-Ni SA/NHCRs to CO_2 molecules. The comparison of calculated free-energy diagrams for eCO_2RR of Ni-C_3N_1 and Ni-C_2N_2 configurations is shown in Fig. 9g, and the energy barrier for the protonation of *CO_2 to *COOH over Ni-C_3N_1 moiety (0.60 eV) is lower than the value of Ni-C_2N_2 structure (0.94 eV), implying that the formation of the key *COOH intermediate is more thermodynamically favorable on Ni-C_3N_1 configuration. These works provide inspiration for designing efficient HSC materials with tailored coordination of single atoms.

Despite most of the current studies being dedicated to improving CO selectivity and suppressing the competitive hydrogen evolution reaction from CO_2 reduction, the production of the mixture of CO and H_2 (syngas) is of great applied relevance. The syngas with specific ratios can serve as the feedstock for the synthetic chemical industry (*e.g.*, Fischer–Tropsch synthesis), especially in the range of 0.25–3.33 CO/H_2.[148] HSC-based materials are reported to function as feasible catalysts for controllable syngas production. For example, Song *et al.*, reported a nitrogen and cobalt co-doped hollow carbon catalyst (Co–HNC), with the Co–C_2N_2 moieties acting as catalytic sites for CO_2 reduction and the N functional groups (*i.e.*, pyridinic and graphitic N) serving as HER sites.[149] The obtained Co-HNC sample showed a faradaic efficiency of nearly 100% and a production rate of ~425 mmol g^{-1} h^{-1} for syngas evolution at −1.0 V *vs.* RHE. Notably, the syngas ratio is close to the desired 1/2 (CO/H_2) that is appropriate for downstream methanol production.[150] The hollow structure and sponge-like thin shell were claimed to be helpful for accelerating the mass transport and maximizing the catalytically active area, rendering the catalyst an excellent electrocatalytic performance. Additionally, in our previous work, a tunable syngas production (CO/H_2 ratio, 1.09 to 2.54) could be achieved from eCO_2RR over a wide electrochemical window from −0.7 to −1.1 V *vs.* RHE, using an aminopolymer-modified hollow carbon sphere incorporating Ag NPs catalyst (Ag-P@HCS).[52] Detailed characterizations suggested that the introduction of aminopolymers led to the finely increased dispersion of Ag NPs and improved CO_2 affinity of Ag-P@HCS, thus optimizing its eCO_2RR performance. The work emphasized the positive effects of aminopolymers in HSC-based eCO_2RR systems.

3.2 Selective production of formate

As an important liquid-phase product of eCO_2RR, formate has extensive applications in the pharmaceutical industry, animal feed, and hydrogen energy transportation.[151] Nowadays, indium (In), copper (Cu), and tin (Sn)-containing catalysts are widely studied in eCO_2RR for CO_2-to-formate production,[152–154] owing to the favorable *OCHO formation and suitable binding intensity with *HCOOH; but some limitations towards pragmatic application still exist, such as unsatisfied selectivity, moderate stability, and large overpotential. In fact, except for the shape and constituent control of the metal/oxides NPs, the electrocatalytic performance is also determined by the electronic and morphologic characteristics of carbon substrates to some extent. Encouragingly, some interesting works have been reported on constructing metal-carbon hollow nano-structured hybrids with space-confinement effects and abundant exposed active sites to address the problems and achieve desirable electro-reactivity. As exemplified by the study conducted by Zhang *et al.*, the pipet-like bismuth (Bi) nanorods semifilled in N-doped carbon nanotubes (Bi-NRs@NCNTs) catalyst (Fig. 10a) delivered a highly efficient CO_2-to-formate electro-conversion,

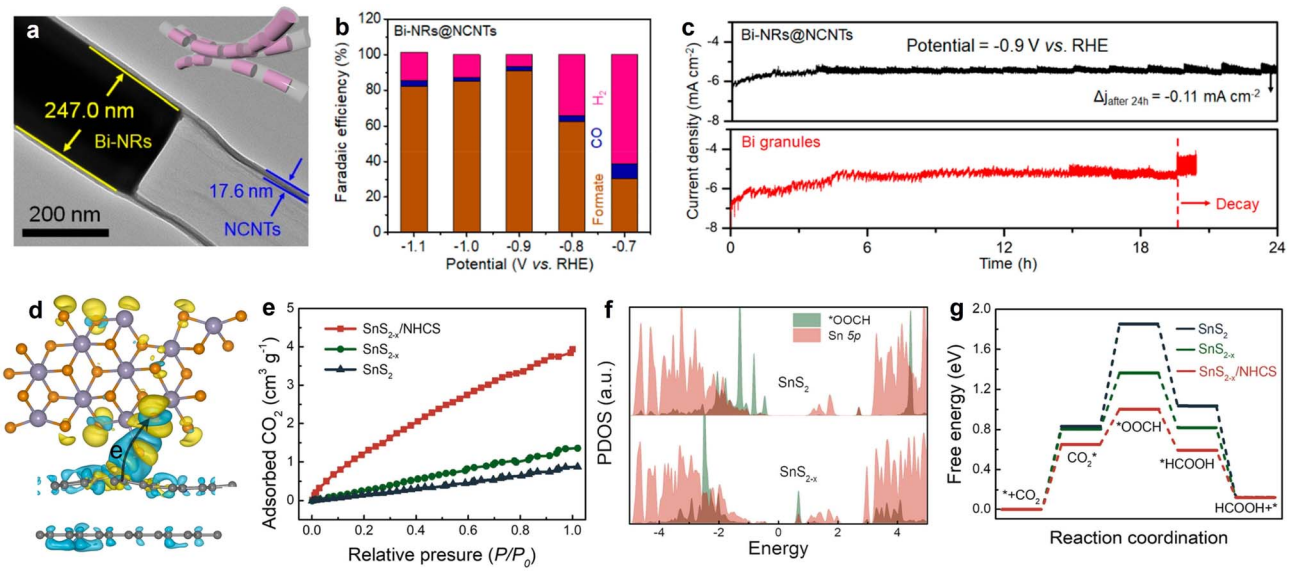

Fig. 10 (a) HRTEM image and morphology illustration (inset) of Bi-NRs@NCNTs. (b) Faradaic efficiencies of the eCO_2RR products of Bi-NRs@NCNTs. (c) Stability comparison of Bi-NRs@NCNTs and Bi granules. Reproduced with permission from ref. 71. Copyright 2021, American Chemical Society. (d) Charge density difference diagram SnS_{2-x}/N-doped carbon. (e) CO_2 adsorption isotherms. (f) Partial density of states (PDOS) of *OOCH and Sn 5p orbital for SnS_2 and SnS_{2-x}. (g) Calculated CO_2RR free energy profiles. Reproduced with permission from ref. 159. Copyright 2022, Elsevier.

showing a high selectivity for formate production with the peak faradaic efficiency value of 90.9% at −0.9 V *vs.* RHE (Fig. 10b).[71] Different from Bi granules, no obvious current density attenuation was observed on Bi-NRs@NCNTs throughout the 24 h electrolysis (Fig. 10c), implying its structural superiority. Specifically, the spatial restriction function of NCNTs efficiently prevents the self-aggregation and oxidation of metallic Bi nanorods, ensuring good durability during long-term testing. Meanwhile, the results demonstrated that the synergy of nanocapillary and nanoconfinement effects induced by NCNTs contributed to the accelerated mass transfer, improved CO_2 adsorption, and concentrated CO_2 around the active sites. This work not only highlights the functions of HSC material in CO_2 valorization, but also provides a promising design philosophy on HSC-based material for energy conversion and beyond.

In another example, Du *et al.* developed a hollow nanostructured hybrid electrocatalyst consisting of Cu, Cu_2O, and nitrogen-doped carbon sphere (HCS/Cu) for highly selective formate production from eCO_2RR.[41] The best-performing sample HCS/Cu-0.12 showed 82.4% $FE_{formate}$ with a current density of 26 mA cm^{-2} at −0.81 V *vs.* RHE, in which the optimized Cu/C heterogenous interfaces could be responsible for the enhanced electron transport and the resulting excellent activity.

Very recently, nitrogen-doped hollow carbon spheres (NHCS) were employed to couple with tin disulfide containing sulfur vacancies to construct a catalyst (SnS_{2-x}/NHCS) with improved CO_2 activation ability and excellent conductivity.[159] DFT simulation analysis confirmed that a migration channel of electrons was built with the direction from NHCS to SnS_{2-x} (Fig. 10d). Benefited from the synergy of S defects and the integration with NHCS, SnS_{2-x}/NHCS exhibited the highest uptake of CO_2 (Fig. 10e). Moreover, simulations of projected density of states (PDOS) for *OOCH and Sn 5p on SnS_{2-x} show a larger overlapping area than on its SnS_2 counterpart, indicating the stronger interaction between *OOCH and SnS_{2-x} (Fig. 10f). In addition, significantly decreased energy barriers for $*CO_2$ formation and *OOCH generation can be observed on SnS_{2-x}/NHCS compared with those of SnS_2 and SnS_{2-x}, signifying the promoted CO_2 activation and conversion capacities (Fig. 10g). As a consequence, the partial current density and faradaic efficiency of SnS_{2-x}/NHCS for formate production increased to 3.4 and 1.2 times, respectively, in comparison to the value of pristine SnS_2. In general, the work disclosed the fundamental correlation between catalyst structure and performance, which may trigger more consideration of the material design by coupling defect engineering and HSC material with matched energy-level structure.

3.3 Selective production of multicarbon products

Of the prevalent eCO_2RR HSC-based electrocatalysts, most mainly produce C1 products (CO or $HCOO^-$), as presented in Table 3. The production of energy-dense and valuable multicarbon (C_{2+}) oxygenates and hydrocarbons, such as ethylene (C_2H_4) and ethanol (C_2H_5OH), is of great value for industrial manufacture, but the relevant reports are relatively rare; the primary obstacle lies in the difficulty of coupling C–C bonds.[161]

Cu-based catalysts are of particular interest in the field of eCO_2RR and are capable of converting CO_2 to a series of C_1/C_2 products. However, suffering from product complexity and unsatisfactory activity, more efficient Cu-based catalysts are required. Considering the structural features of HSC materials for the carbonaceous intermediates, Pan *et al.* designed hollow mesoporous carbon spheres confining Cu cluster catalyst (Cu/HMCS) for improving the C_2 selectivity.[37] *In situ* Fourier transform infrared spectroscopy (FTIR) analysis revealed that, under the aid of nanoconfinement provided by HMCS, with suitable Cu cluster loading, the conversion of *CO to *CHO could be facilitated; additionally, the nanocavity protection effects of HMCS allowed to boost the C–C bond coupling to generate C_2 products. As a result, the sample (Cu/HMCS-20%) with optimized conditions exhibits a C_2 (C_2H_4 and C_2H_5OH) faradaic efficiency of 88.7% at −1.0 V *vs.* RHE. This work provides insights for designing robust catalysts with high C_2 selectivity.

In addition to hollow carbon spheres, carbon nanotubes (CNTs) are also commonly used in electrocatalysis; they can not only offer excellent conductivity, but also prevent the agglomeration of catalytic components.[162] Liu *et al.* investigated the surface modification of N-doped CNTs on Cu_2O NPs for enhanced CO_2-to-C_2 electro-conversion.[160] The Cu_2O NPs-NCNT sample showed a maximal C_2 (C_2H_4 and C_2H_5OH) faradaic efficiency of 77.61% at −1.1 V *vs.* RHE, suppressing the value of the NCNT-free sample (Cu_2O NPs, FEC_2 38.15%); noteworthily, the C_2 partial current density of Cu_2O NPs-NCNT (16.79 mA cm^{-2}) is 7.30 folds higher than that of Cu_2O NPs (2.30 mA cm^{-2}) at the same applied potential. It is proposed that NCNT is helpful for catalyzing the conversion of CO_2 to CO, which subsequently enriches the CO concentration at the heterogeneous interface of NCNT and Cu_2O NPs and is conducive to C–C coupling to generate C_2 products.

Recently, some strategies (*e.g.*, alloying and surface doping) have been demonstrated to enhance the FE towards C_{2+} production of Cu materials. For instance, Chen *et al.* reported Cu–Ag tandem alloy catalysts, and the results illustrated that the CO-enriched environment introduced by Ag facilitated the subsequent C–C coupling processes occurring at the Cu sites, thereby enhancing the formation of C_{2+}.[163] Additionally, Wu *et al.* found that employing molecular doping strategies, including the introduction of aromatic heterocycles (*e.g.*, thiadiazole and triazole derivatives) to CuAg alloy, can orient the reaction route towards C_{2+} production, achieving a high FE of C_{2+} ($\approx$80%); detailed analyses demonstrated that the functional groups with electron-withdrawing feature are capable of modulating the electronic structure of Cu atoms and thereby enhancing the catalytic reaction rate.[164] In general, incorporating modern strategies such as alloying and molecular doping into the design of copper-containing HSC-based catalysts, alongside the optimization of component interactions, holds the potential to further enhance the efficiency of catalyzing C_{2+} production and accelerate the pace of approaching practical application.

4. Thermocatalytic CO_2 conversion of hollow carbon-based materials

Thermocatalytic CO_2 conversion to produce commodity chemicals is a promising way to alleviate the dependence on fossil resources; it can be classified as hydrogenation and reforming routes loosely. For the reforming reaction, CO_2 serves as an oxidant for catalytically reforming methane to generate syngas (CO and H_2) under high temperature condition (600–1000 °C).[10] Nevertheless, the extremely high temperature of the reforming reaction may lead to the decomposition of the carbon material; and there are few researches of HSC-related material reported in this field. As for CO_2 hydrogenation, it refers to the conversion of CO_2 with H_2 to formic acid, methane and olefins, *etc.*, under a relatively mild ambient condition. CO_2 hydrogenation is in line with the concept of green chemistry, and holds important industrial application prospects, therefore, many efficient HSC-based materials were designed for this reaction (Table 4). In this section, the recent applications of HSC-based materials in relatively popular CO_2 hydrogenation applications will be summarized and discussed.

4.1 CO_2 hydrogenation to formate

Formate synthesis from CO_2 hydrogenation is regarded as one of the most sustainable and economically feasible for utilization of CO_2. However, designing efficient catalysts with high stability for formate production from CO_2 hydrogenation is challenging because of the difficulty of CO_2 activation and harsh reaction conditions. In this regard, our group has developed a series of hollow carbon sphere-based materials *via* rationally engineering the catalyst component/structure, and achieved desirable performance. Compared to the conventional supported material, encapsulation effects of the cavity in hollow carbon spheres efficiently prevent the leaching of some functionalized modifiers (*e.g.*, aminopolymer) and the active metals, resulting in improved robustness and formate conversion efficiency. To begin with, a nanostructured catalyst consisting of sub-3-nm-sized PdAg NPs with high dispersity and aminopolymers encapsulated in mesoporous hollow carbon spheres (PdAg-P@MHCS) was synthesized (Fig. 11a–e).[51] MHCS provided immobilization spaces for aminopolymers; and the amine groups of polymers promoted the metal ions adsorption, enabling the selective formation of PdAg NPs within P@MHCS. As a result, the turnover number (TON) of optimized PdAg-P@MHCS for formate production reached 2680 at 100 °C for 24 h. With the combination of experimental characterization and kinetics analysis, the possible reaction mechanism was proposed, as illustrated in Fig. 11f. Firstly, H_2 dissociation occurs and further forms Pd-hydride species, which are active in the hydrogenation process (step 1). Then, the bicarbonate (HCO_3^-) adsorbs onto Ag atoms that are in an electron-deficient state after alloying with Pd (step 2); meanwhile, CO_2 dissolution in the alkaline reaction solution continuously provides HCO_3^- (step 3). The dissociative formate is formed under the attack of active H to HCO_3^- adsorbed on Ag (step 4). This work demonstrated a new design strategy for developing highly efficient CO_2 hydrogenation catalysts for formate production.

To alleviate the use of hazardous reagents (*i.e.*, carbon tetrachloride) and the complex operation procedures in the aforementioned work, we further exploited a novel and facile synthesis method for monodispersed N-doped microporous hollow carbon spheres encapsulating PdAg alloy catalyst *via* an ethylenediamine-assisted pyrolysis.[36] And it showed competitive CO_2 hydrogenation activity with the TON value of 2750 at 100 °C for 24 h.

In addition to alloy, the MHCS was also employed to confine a composite of mononuclear Ru^{3+} and N, P-containing porous organic polymers (Ru^{3+}-POPs) in another study of ours (Fig. 11g).[50] The Ru^{3+}-POPs@MHCS catalyst with optimized content of Ru^{3+}-POPs exhibited good activity for CO_2 hydrogenation to formate (TON = 1228 at 100 °C for 24 h), surpassing that of Ru^{3+}-POPs (without MHCS) sample (Fig. 11h). The superior performance originated from the promoted adsorption abilities of CO_2 and H_2 induced by MHCS, as evidenced by the kinetics analysis (Fig. 11i and j). Furthermore, the Arrhenius curve displayed that the activation energy of hydrogenated CO_2-to-formate conversion decreased with Ru^{3+}-POPs being encapsulated in MHCS (Fig. 11k). Based on the above discussion and reasoning, we demonstrate here that hollow carbon spheres benefit the overall performance of formate production from CO_2 hydrogenation. The optimization of nanoconfined space is still worthy of further study, and our relevant researches are in progress.

4.2 CO_2 methanation

Methane synthesis from CO_2 hydrogenation ($CO_2 + 4H_2 \rightarrow CH_4 + 2H_2O$, $\Delta H^\circ = -165$ kJ mol^{-1}), known as the Sabatier reaction, is an exothermic process that is more thermodynamically favorable than many other hydrogenation routes.[21,171] However, it still suffers from significant kinetic limitations due to the intrinsical inertness of linear CO_2 and the involvement of an eight-electron transfer process.[165,172,173] Several metal-containing catalysts have been demonstrated as effective candidates for this reaction, typically based on Ru, Rh, Pd, and Ni NPs on supported materials, with Ni-based catalysts being the most popular one because of the low cost and rich reserves.[174–176] Nevertheless, the high temperature in the catalytic reaction may give rise to issues of stability and sintering in Ni-based catalysts. The incorporation of hollow structured carbon enables the encapsulation or embedding of metal sites inside its structure, which can effectively alleviate the problems of coke formation and metal sintering, and ultimately improve the activity, stability, and selectivity for methane synthesis from CO_2 hydrogenation.[42,177] For instance, Lin *et al.*, presented a MOF-derived hollow carbon nanostructured catalyst encapsulating dispersed Ni nanoparticles (Ni@C) which affords better CO_2 methanation performance than Ni/C (control sample, Ni NPs on graphite carbon) owing to the unique carbon-confined configuration.[166] Additionally, no obvious deactivation of Ni@C catalyst was observed in the long-term stability test at 250 °C for 24 h; in contrast, Ni/C without carbon shell protection displayed a 50% decline in CH_4 yield by 24 h.

Table 4 Summary of HSC-based catalysts for thermocatalytic CO_2 conversion

Catalyst	Target product	Reaction condition	Catalytic performance	Ref.
NiCe/CNT	CH_4	0.1 g catalyst, 350 °C, atmospheric pressure, $H_2/CO_2 = 4:1$ (flow rate), continuous fixed-bed, gas hourly space velocity (GHSV) = 30 L g_{cat}^{-1} h^{-1}	CO_2 conversion rate: 83.8% Selectivity: 99.8%	165
Ni NPs/N-CNT	CH_4	0.2 g catalyst, 360 °C, atmospheric pressure, $H_2/CO_2 = 6:1$, continuous fixed-bed, GHSV = 120 L g_{cat}^{-1} h^{-1}	CO_2 conversion rate: 92% Selectivity: 98%	45
Ni NPs@carbon hollow sphere	CH_4	0.1 g catalyst, 325 °C, atmospheric pressure, $H_2/CO_2 = 4:1$, fixed-bed flow reactor, GHSV = 33 L g_{cat}^{-1} h^{-1}	CO_2 conversion rate: ~100% Selectivity: 99.9%	166
Ni NPs/NCNT	CH_4	0.04 g catalyst, 340 °C, atmospheric pressure, $H_2/CO_2/Ar = 4:1:0.6$, fixed-bed flow reactor, GHSV = 50 L g_{cat}^{-1} h^{-1}	CO_2 conversion rate: ~50% Selectivity: 95%	42
Ni NPs/NCNT	CH_4	0.1 g catalyst, 400 °C, atmospheric pressure, $H_2/CO_2/He = 4:1:5$, weight hourly space velocity (WHSV) = 60 L g_{cat}^{-1} h^{-1}	CO_2 conversion rate: 81.2% Selectivity: 99.2%	162
PdAg-aminopolymer@MHCS	Formate	100 °C, 2 MPa (1 MPa H_2 and 1 MPa CO_2), 15 mL 1.0 M $NaHCO_3$ aqueous reaction solution, closed reactor, 24 h	Turnover number (TON): 2680 Turnover frequency (TOF): 112 h^{-1}	51
PdAg@NHCS	Formate	100 °C, 2 MPa (1 MPa H_2 and 1 MPa CO_2), 15 mL 1.0 M $NaHCO_3$ aqueous solution, closed reactor, 24 h	TON: 2750 TOF: 115 h^{-1}	36
PdCu@MHCS	Formate	100 °C, 2 MPa (1 MPa H_2 and 1 MPa CO_2), 15 mL 1.0 M $NaHCO_3$ aqueous solution, closed reactor, 24 h	TON: 1432 TOF: 60 h^{-1}	49
Ru^{3+}-N,P-containing porous organic polymers@MHCS	Formate	120 °C, 4 MPa (2 MPa H_2 and 2 MPa CO_2), 7.8 mL 1.0 M $NaHCO_3$ aqueous solution, closed reactor, 24 h	TON: 1228 TOF: 51 h^{-1}	50
Ru/N-MHCS	Formate	120 °C, 8 MPa (4 MPa H_2 and 4 MPa CO_2), 40 mL 3 M aqueous Et_3N solution, closed reactor, 2 h	TON: 7550 TOF: 3775 h^{-1}	118
Fe@CNTs	C_{2+} products	0.4 g catalyst, 370 °C, atmospheric pressure, $H_2/CO_2 = 3:1$ (flow rate), fixed-bed reactor	CO selectivity: 45.1% CH_4 selectivity: 29.3% C_2–C_4 selectivity: 24.3% C_{5+} selectivity: 1.3%	167
FeZn-NC (Fe@C matrix)	C_{2+} products	0.5 g catalyst, 320 °C, 3 MPa, $H_2/CO_2 = 3:1$ (molar ratio), fixed-bed reactor, space velocity = 7200 mL g^{-1} h^{-1}, 5 h	CO selectivity: 19.9 C mol% CH_4 selectivity: 16.6 C mol% Long-chain hydrocarbons (C_{5+}) selectivity: 27.4 C mol% Ligh olefins (C_2–$C_4^=$) selectivity: 30.0 C mol%	168
FeZnK-NC (Fe inserted in carbon shell)			CO selectivity: 21.2 C mol% CH_4 selectivity: 19.1 C mol% C_{5+} selectivity: 22.1 C mol% C_2–$C_4^=$ selectivity: 32.0 C mol%	
FeK/SWNT	C_{2+} products	0.2 g catalyst, 340 °C, 2 MPa, $H_2/CO_2/N_2 = 72:24:4$ (volume ratio), fixed-bed reactor, GHSV = 9000 mL g_{cat}^{-1} h^{-1}, 24 h	Olefins selectivity = 62.3% ($C_{5+}^=$ selectivity = 39.8%, C_2–$C_4^=$ selectivity = 22.5%) FTY (iron-time yield) for heavy olefins = 26.5 μmol_{CO2} g_{Fe}^{-1} s^{-1}	169
FeK/MWNT			Olefins selectivity = 52.5% ($C_{5+}^=$ selectivity = 21.8%, C_2–$C_4^=$ selectivity = 30.7%) FTY (iron-time yield) for heavy olefins = 10.2 μmol_{CO_2} g_{Fe}^{-1} s^{-1}	
Spark plasma sintered Fe/CNTs	C_{2+} products	0.5 g catalyst, 350 °C, 8.5 MPa, $H_2/CO_2 = 2:1$, fixed-bed reactor, GHSV = 14.4 L g_{cat}^{-1} h^{-1}	CO selectivity = 18 mol% CH_4 selectivity = 35 mol% C_{2-4} selectivity = 35 mol% C_{5+} selectivity = 12 mol% Iron-time yield = 12.2 mol_{CO_2} g_{Fe}^{-1} s^{-1}	170

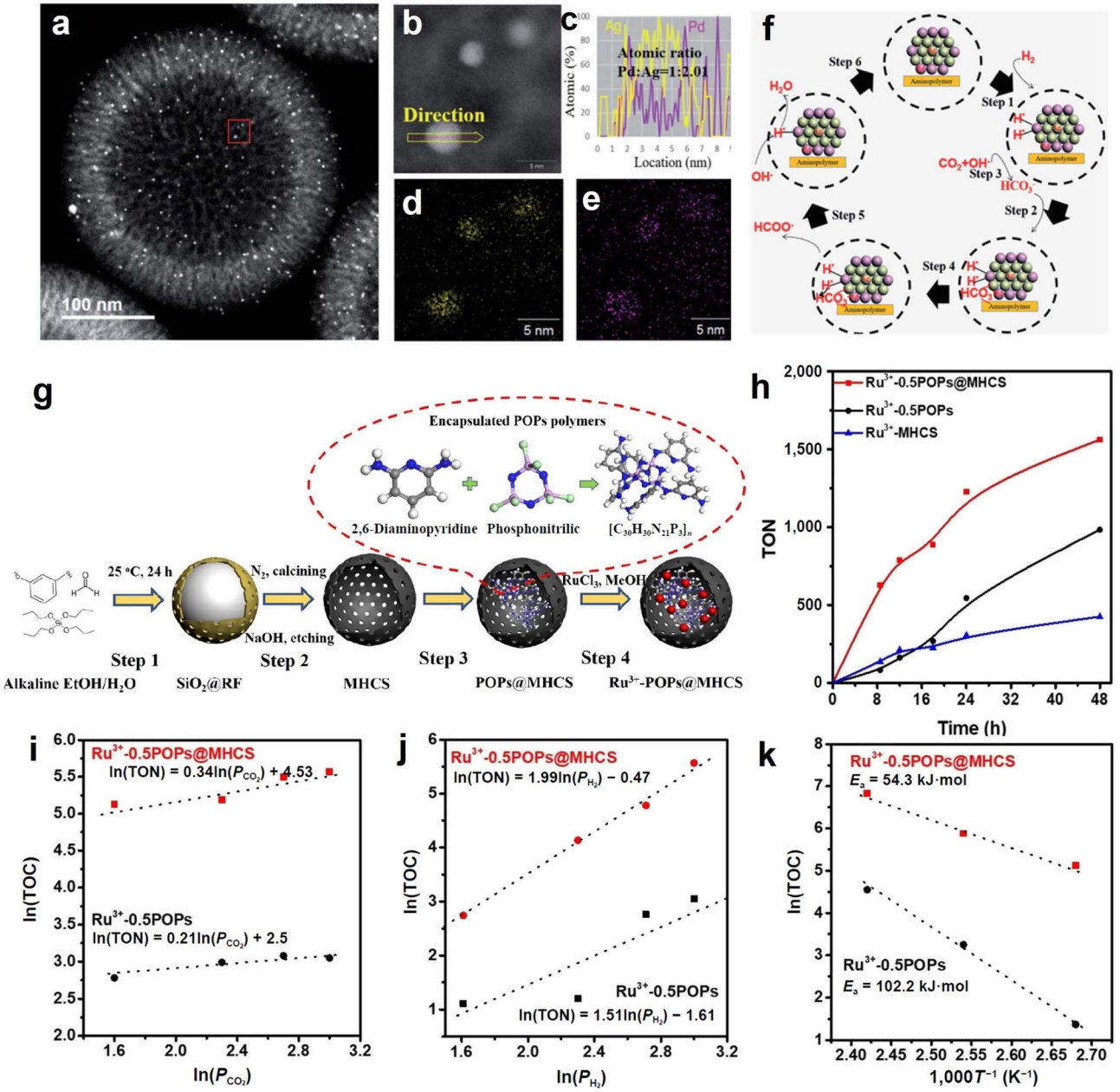

Fig. 11 (a) HAADF-STEM image of PdAg-P@MHCS. (b) Magnified image of the red frame zone in (a). (c) Elemental line scan across the PdAg NPs in (b). (d and e) Elemental maps of (d) Ag and (e) Pd. (f) Hydrogenated CO_2-to-formate conversion pathway over PdAg-P@MHCS catalyst. Reproduced with permission from ref. 51. Copyright 2020, Royal Society of Chemistry. (g) Synthesis of Ru^{3+}-POPs@MHCS catalyst. (h) Reaction time profile of hydrogenated CO_2-to-formate conversion over the as-prepared samples. (i–k) Double logarithm plots of TON and the partial pressure of (i) CO_2 and (j) H_2 in the hydrogenation process, and (k) Arrhenius plots over optimized Ru^{3+}-0.5POPs@MHCS and Ru^{3+}-0.5POPs (MHCS-free) samples. Reproduced with permission from ref. 50. Copyright 2021, Tsinghua University Press and Springer-Verlag GmbH Germany, part of Springer Nature.

Generally, the excessive local heat generated during CO_2 methanation may result in the formation of "hot spots" that affect the stability duration and methane selectivity. Introducing an appropriate carbon material with good thermal conductivity can benefit the uniform dispersion of the reaction heat and ensure the methanation process. For example, Wang *et al.* reported that Ni NPs decorated N-doped carbon nanotubes (N-CNT) catalyst (Ni/N-CNT) (Fig. 12a and b) exhibited high methane selectivity of 98% and CO_2 conversion rate of 92%, even at a high gas hourly space velocity (GHSV) of 120 000 mL g^{-1} h^{-1} with a H_2-to-CO_2 v/v ratio of 6 (Fig. 12c).[45] The existence of N-CNT with unique characteristics contributed to the superior performance because (1) the excellent thermal conductivity limited the generation of local "hot spots", (2) the nanotube configuration optimized the diffusion pathway of the reactants, and (3) the alkalized surface of N-CNT is favorable for

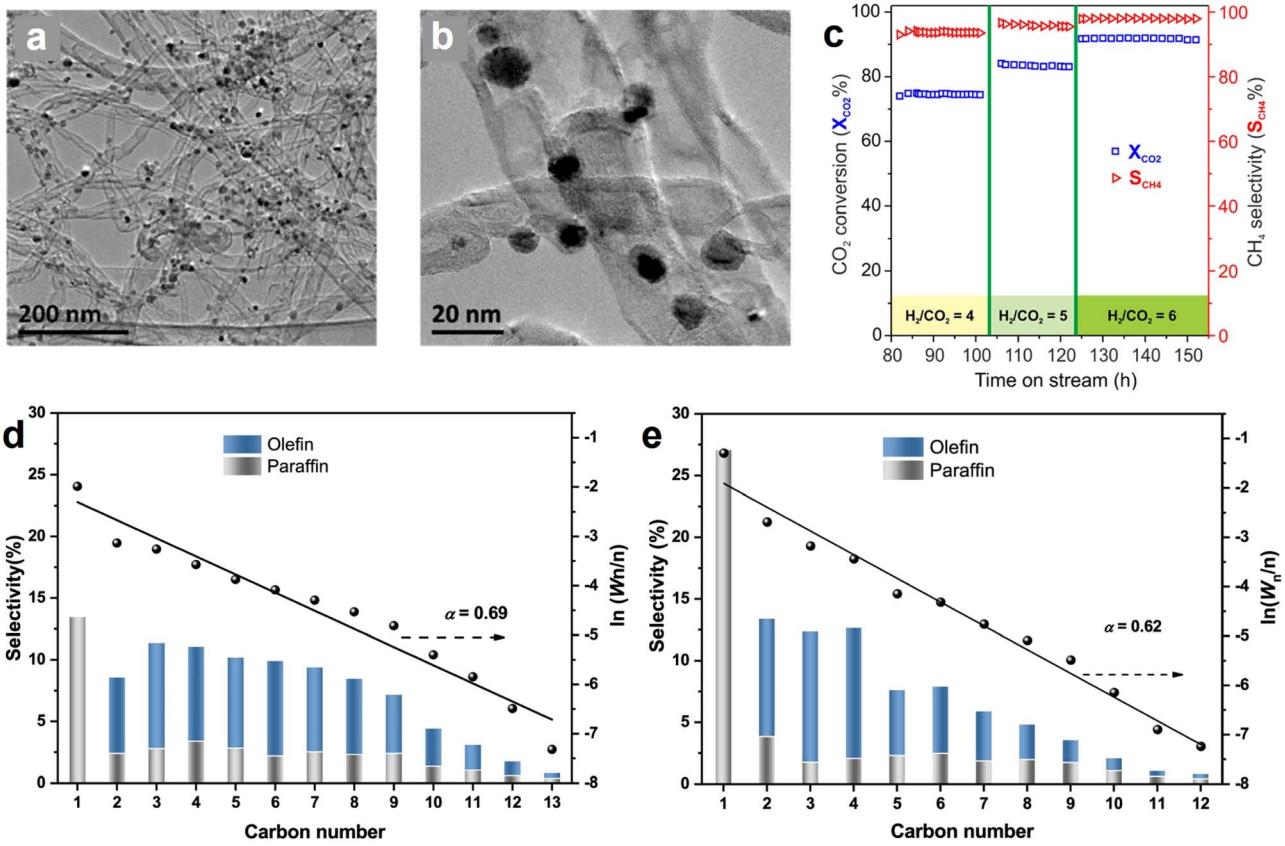

Fig. 12 (a and b) TEM images of Ni/N-CNT catalyst in different magnifications. (c) Influence of H_2/CO_2 ratio on the CO_2 methanation activity and selectivity Ni/N-CNT catalyst at a GHSV of 120 000 mL g^{-1} h^{-1}. Reproduced with permission from ref. 45. Copyright 2018, American Chemical Society. Hydrocarbon production distributions over the (d) FeK/SWNTs and (e) FeK/MWNTs catalysts after CO_2 hydrogenation test for 24 h. Reaction conditions: 0.2 g of catalyst, $T = 613$ K, $P = 2.0$ MPa, $H_2/CO_2 = 3$, GHSV = 9000 mL g_{cat}^{-1} h^{-1}. Anderson–Schulz–Flory (ASF) plots and α-values (chain propagation probability) are also presented; W_n represents the weight fraction of a hydrocarbon with n carbon atoms. Reproduced with permission from ref. 169. Copyright 2021, American Chemical Society.

concentrating CO_2 in the proximity of catalytically active Ni sites. Recently, another study disclosed the importance of N-doping catalyst towards CO_2 methanation, and the results demonstrated that N-doping enabled the formation of highly dispersive Ni sites that were responsible for the enhanced performance.[162] Inspired by these intriguing studies, in our opinion, it is deemed to be of great significance to conduct more comprehensive investigations of the metal–support interaction, namely, the correlation between the intrinsic characteristics of hollow carbon internal/external surfaces and the active metals.

4.3 CO_2 hydrogenation to multicarbon products

Among the potential products from CO_2 hydrogenation, C_{2+} hydrocarbon products such as olefins and paraffins are of particular interest due to their large energy density and industrial relevance.[178,179] CO_2 hydrogenation to hydrocarbons commonly involves reverse water–gas shift (RWGS) reaction and subsequent Fischer–Tropsch synthesis (FTS); the tandem of these two processes is thermodynamically feasible, but requires an effective catalyst to drive.[180] The carbon-supported Fe-based catalysts receive considerable attention because they show good activity in both RWGS and FTS.[168,181] For the potential hollow carbon support candidates, the CNTs with tubular morphology is the most popular one, owing to their good adhesion to metal NPs, high mechanical strength, good thermal conductivity, and ease of surface functionalization.[182,183]

In 2013, Fe NPs@CNT catalyst was proved to be active for CO_2 hydrogenation to produce hydrocarbons by O'Byrne *et al.*, but the C_{2+} products selectivity and iron time yield (FTY) were relatively low.[167] Encouragingly, an iron–potassium catalyst supported on single-wall carbon nanotubes (FeK/SWNT) reported by Wang *et al.* delivered an extremely competitive CO_2 hydrogenation performance, with the olefins selectivity achieving 62.3%, where the heavy olefins ($C_{5+}^{=}$) selectivity and light olefins (C_2–$C_4^{=}$) were 39.8% and 22.5%, respectively.[169] Fig. 12d and e show the comparison of CO_2 hydrogenation results after 24 h measurement over FeK/SWNT and FeK/MWNT (control sample with multi-walled carbon nanotubes). According to the distribution of the hydrocarbons, both of the samples show higher selectivity for olefins instead of paraffins. Notably, FeK/SWNTs favor the formation of heavy olefins, whereas the production of light olefins is preferred on FeK/MWNT (see Table 4 Row 14 and 15 for more details), as reflected by the larger α-values (chain propagation probability)

of FeK/SWNTs (0.69) as compared to that of FeK/MWNT (0.62). Detailed characterizations demonstrated that the excellent catalytic activity of FeK/SWNTs catalyst was associated with the presence of SWNTs with large curvature, which manipulated the electron distribution[184] and accelerated the dissociation of CO on Hägg carbide, eventually boosting CO_2 hydrogenation to heavy olefins. In extension to the conventional CNTs, the dense CNT materials are suitable for specific catalytic applications. Chernyak *et al.* prepared a new type of densely packed CNTs with embedding Fe NPs catalyst (Fe/CNT) *via* a spark plasma sintering method.[170] Under supercritical conditions (350 °C, 8.5 MPa), the catalyst exhibited high specific activities at low H_2/CO_2 ratios (1 or 2), with the iron-time yields of 5.4–12.2 $mol_{CO_2}\ g_{Fe}^{-1}\ s^{-1}$ and C_{2+} products selectivity of 40–50 mol%, in CO_2 hydrogenation without pretreatment. This work highlighted the importance of CNT support with increased density for stabilizing the Fe NPs, which contributed to the strong metal–support interaction and CO intermediate activation.

Apart from the catalyst modification, the rational design of thermocatalytic reactors for CO_2 reduction also contributes to enhancing catalytic activity and selectivity. It is recommended to establish an appropriate dynamic mathematical model to comprehend heat conduction and mass transfer during the reaction process. Furthermore, computational fluid dynamics analysis can be employed to investigate parameters such as fluid flow and pressure drop. The integration of dynamic mathematical models, computational simulation tools, and experimental validation can guide the development of efficient thermocatalytic CO_2 reduction systems.

5. Conclusion and outlook

Herein, the recent progress of HSC-based materials in the fields of electrocatalytic and thermocatalytic CO_2 utilization has been reviewed. The synthetic methods of HSC were first introduced. Then, a comprehensive overview of functionalization strategies for HSC was provided, including nonmetal doping, metal single atom anchoring, and metal nanoparticle modification; and they were found to offer numerous benefits, such as optimization of electronic structure, superior CO_2 adsorption affinity, and improved reaction intermediate activation, allowing for the efficient enhancement of overall catalytic CO_2 conversion behavior. Finally, the discussion of HSC-based materials towards electrocatalytic and thermocatalytic CO_2 conversion applications was presented, based on the CO_2 reduction product category. While encouraging progress has been witnessed in these fields, some key issues still exist that merit further study.

(1) The synthesis of HSC materials with good rigidity, homogeneous morphology, and favorable reproducibility is mostly dependent on the utilization of the hard template method. However, this approach involves the use of highly corrosive agents to remove the template, potentially leading to adverse environmental consequences. Hence, the development of a green and environmentally friendly synthesis for high-quality HSC is urgently needed.

(2) The regulation of the pore structure of HSC is an important issue, as the porosity can affect the mass transport and the number of active sites, both of which have large influences on the activity and product selectivity. As exemplified by the work from Cao *et al.*, in Ni–N doped hollow carbon sphere catalyst system used for eCO_2RR, the mesopores on carbon shell were found to be favorable for the CO_2 diffusion; while the micropores with confinement effect were conducive to the formation of Ni–N active sites during the synthesis process. By balancing the content of micropore and mesopore, the CO_2-to-CO reaction rate can be efficiently improved.[38] In thermocatalytic CO_2 hydrogenation, the carbon-supported Fe–Co–K oxide catalyst using carbon support containing both micropores and mesopores shows higher olefin selectivity, as compared to that of the analogue with only micropores; the results suggest that the mesopores with sufficient accommodation space enable control over the intimate contact of K and Fe_xO_y species, making it possible to realize the boosted olefin production.[185]

(3) Most of the works are rather ambiguous in describing the contribution of confinement effects of HSC to the enhanced catalytic performance, which should be clarified. Here are some good examples. In CO_2 electroreduction, the confinement effects of hollow carbon spheres contribute to the pH modulation of the internal cavity, which inhibits the competitive hydrogen evolution reaction by controlling the rate of H^+ replenishment and creating a localized alkaline environment in the proximity of the catalytically active sites.[46] In thermocatalytic CO_2 reduction, in addition to improving the dispersion and stability of metal nanoparticles, HSC contributes to concentrating CO_2 around the catalytically active sites and thus accelerating the reaction rate.[45] In our opinion, more research efforts should be placed on emphasizing and clarifying the relationship between the confinement structure, active site, and substrate molecule, which allows to better utilize the positive effects and develop more advanced catalysts.

(4) Currently, the research on single-atom-based HSC materials is mainly focused on CO_2 electroreduction, and only few cases in thermocatalytic CO_2 conversion because the stabilization of single atoms with high surface free energy is a major challenge under the harsh conditions of thermocatalysis. Notably, in some specific situations, single atoms exhibit surprising stability, even better than metal nanoparticles. For example, the transformation of metal nanoparticles (Ru, Rh, and Pd) can be achieved by phosphine (PH_3)-assisted pyrolysis to form single-atom materials, in which single-atom species are firmly fixed on thermodynamically stable sites, which help inhibit the agglomeration and leakage of single-atom species.[186] Additionally, there are some studies reported the thermal atomic capture method allows the conversion of noble metal Pd, Pt, and Au nanoparticles to thermally stable single atoms.[187,188] As a result, the stabilized single atoms showed better catalytic performance than nanoparticles; these works may offer some inspiration for the development of stable single-atom-based HSC materials for thermocatalytic CO_2 conversion.

(5) Furthermore, the types of single-atom-related HSC catalysts are limited, with the majority of them focusing only on Ni or Co single atoms in eCO_2RR for CO production (Table 3), and

it is important to further exploit high-performance catalysts. In this regard, the following aspects are worthy of further consideration. To begin with, novel active metal single atoms are suggested to be introduced into the matrix of HSC material. For instance, the fluxional property of gallium (Ga) has been proven to be utilized to efficiently enhance eCO_2RR behavior;[189] the analogous unique characteristics of more single atoms need to be explored. Secondly, studies on the coordination environment of the central metal atom should be conducted, because the coordinated non-metal atoms can affect the electronic structure of the central metal atom, resulting in the change of the adsorption/activation ability towards reactant molecules. Thirdly, rationally designing dual single-atom sites with different functions is helpful in realizing some complex tandem reactions and in achieving the controllable production of specific products.

(6) HSC materials possess unique cavities and abundant pore structures, which provide a flexible platform for designing multifunctional catalysts. Integrating with other novel materials, the hybrid catalyst suitable for various catalytic application scenarios can be expected. As an example, the novel high-entropy alloys are active for both eCO_2RR[128] and thermocatalytic CO_2 hydrogenation.[190] Combining similar materials with HSC carbon materials to develop novel catalysts is also a research direction of interest.

(7) During the processes of electro-/thermocatalytic CO_2 conversion, the intrinsic structure of the HSC materials may be changed under harsh conditions, such as large applied potential or high temperature. In this regard, *ex situ* characterizations may not be able to accurately characterize the catalysts; therefore, *in situ* measurements, such as *in situ* XAFS, Raman, XRD, and DRIFTS, should be employed to dynamically assess the structural change, which enables the guidance of a reasonable HSC material design. Theoretical simulation is a powerful tool to uncover catalytic mechanisms. Except for the commonly used DFT theoretical simulation, finite element modeling[191,192] and molecular dynamics[193,194] simulations are recommended to understand the mass transport behavior during the catalytic CO_2 reduction reaction.

(8) The continuous exploration of the unique properties of HSC materials has pushed their application boundaries. For instance, a recent study revealed that HSC played an important role in enhancing photocatalytic CO_2 reduction performance in a ternary HSC/CdS@$ZnIn_2S_4$ photocatalyst by offering multiple benefits, including improved light harvesting, increased CO_2 adsorption, protection of CdS against photocorrosion, *etc.*[195] In another work, HSC was demonstrated to be effective in boosting the separation of photoexcited electron–hole pairs and providing more catalytically active sites in the g-C_3N_4/Bi_2O_3@-HSC photocatalyst system; as a result, enhanced photocatalytic antibiotic degradation can be achieved.[196] In fact, the carbon shell of HSC material can absorb and convert light to heat under irradiation, resulting in the formation of a local hotspot, which is helpful for boosting the reaction kinetics.[197] As there is a lack of relevant reports, further study on the photo-thermal features of HSC and the development of HSC-based photothermal catalytic reactors will be of great significance.

The unprecedented development of HSC-based materials in recent years provides infinite possibilities for sustainable CO_2 utilization. We expect that this timely review will bring fellow researchers some inspiration to design more advanced HSC-based materials.

Author contributions

All of the authors contributed to the manuscript preparation. K. L. and Y. K. conceived the outline of the manuscript. K. L. wrote the original draft of the manuscript. Y. K. and H. Y. discussed and helped revise the manuscript.

Conflicts of interest

There are no conflicts to declare.

Acknowledgements

Y. K. and H. Y. gratefully acknowledge the Grants-in-Aid for Scientific Research from the Japan Society for the Promotion of Science (JSPS) (grant no. 22H00275). Y. K. acknowledges the cooperative research program of "Network Joint Research Center for Materials and Devices" (no. 20231065). K. L. gratefully acknowledges the financial support from the China Scholarship Council (No. 202108420065).

References

1 W. Gao, S. Liang, R. Wang, Q. Jiang, Y. Zhang, Q. Zheng, B. Xie, C. Y. Toe, X. Zhu, J. Wang, L. Huang, Y. Gao, Z. Wang, C. Jo, Q. Wang, L. Wang, Y. Liu, B. Louis, J. Scott, A. C. Roger, R. Amal, H. He and S. E. Park, *Chem. Soc. Rev.*, 2020, **49**, 8584–8686.
2 D. I. A. McKay, A. Staal, J. F. Abrams, R. Winkelmann, B. Sakschewski, S. Loriani, I. Fetzer, S. E. Cornell, J. Rockström and T. M. Lenton, *Science*, 2022, **377**, eabn7950.
3 J. Rogelj, M. Den Elzen, N. Höhne, T. Fransen, H. Fekete, H. Winkler, R. Schaeffer, F. Sha, K. Riahi and M. Meinshausen, *Nature*, 2016, **534**, 631–639.
4 M. G. Lawrence and S. Schäfer, *Science*, 2019, **364**, 829–830.
5 M. Meinshausen, J. Lewis, C. McGlade, J. Gütschow, Z. Nicholls, R. Burdon, L. Cozzi and B. Hackmann, *Nature*, 2022, **604**, 304–309.
6 M. B. Ross, P. De Luna, Y. Li, C. T. Dinh, D. Kim, P. Yang and E. H. Sargent, *Nat. Catal.*, 2019, **2**, 648–658.
7 Y. Dong, P. Duchesne, A. Mohan, K. K. Ghuman, P. Kant, L. Hurtado, U. Ulmer, J. Y. Y. Loh, A. A. Tountas, L. Wang, F. M. Ali, M. Xia, R. Dittmeyer and G. A. Ozin, *Chem. Soc. Rev.*, 2020, **49**, 5648–5663.
8 H. Ou, G. Li, W. Ren, B. Pan, G. Luo, Z. Hu, D. Wang and Y. Li, *J. Am. Chem. Soc.*, 2022, **144**, 22075–22082.
9 S. Wang, L. Wang, D. Wang and Y. Li, *Energy Environ. Sci.*, 2023, **16**, 2759–2803.
10 S. Das, J. Pérez-Ramírez, J. Gong, N. Dewangan, K. Hidajat, B. C. Gates and S. Kawi, *Chem. Soc. Rev.*, 2020, **49**, 2937–3004.

11 S. Garg, M. Li, A. Z. Weber, L. Ge, L. Li, V. Rudolph, G. Wang and T. E. Rufford, *J. Mater. Chem. A*, 2020, **8**, 1511–1544.
12 C. J. Chang, Y. A. Lai, Y. C. Chu, C. K. Peng, H. Y. Tan, C. W. Pao, Y. G. Lin, S. F. Hung, H. C. Chen and H. M. Chen, *J. Am. Chem. Soc.*, 2023, **145**, 6953–6965.
13 X. Wang, Y. Jiang, K. Mao, W. Gong, D. Duan, J. Ma, Y. Zhong, J. Li, H. Liu, R. Long and Y. Xiong, *J. Am. Chem. Soc.*, 2022, **144**, 22759–22766.
14 T. Wang, J. Wang, C. Lu, K. Jiang, S. Yang, Z. Ren, J. Zhang, X. Liu, L. Chen, X. Zhuang and J. Fu, *Adv. Mater.*, 2023, **2205553**, 1–8.
15 Y. Hao, F. Hu, S. Zhu, Y. Sun, H. Wang, L. Wang, Y. Wang, J. Xue, Y. F. Liao, M. Shao and S. Peng, *Angew. Chem., Int. Ed.*, 2023, **62**, e202304179.
16 X. Tan, S. Jia, X. Song, X. Ma, J. Feng, L. Zhang, L. Wu, J. Du, A. Chen, Q. Zhu, X. Sun and B. Han, *Chem. Sci.*, 2023, **14**, 8214–8221.
17 H. Jiang, L. Wang, H. Kaneko, R. Gu, G. Su, L. Li, J. Zhang, H. Song, F. Zhu, A. Yamaguchi, J. Xu, F. Liu, M. Miyauchi, W. Ding and M. Zhong, *Nat. Catal.*, 2023, **6**, 519–530.
18 W. Ren, X. Tan, W. Yang, C. Jia, S. Xu, K. Wang, S. C. Smith and C. Zhao, *Angew. Chem., Int. Ed.*, 2019, **58**, 6972–6976.
19 C. S. Diercks, Y. Liu, K. E. Cordova and O. M. Yaghi, *Nat. Mater.*, 2018, **17**, 301–307.
20 Y. Chen, Y. Yao, Y. Xia, K. Mao, G. Tang, Q. Wu, L. Yang, X. Wang, X. Sun and Z. Hu, *Nano Res.*, 2020, **13**, 2777–2783.
21 M. Kosari, A. M. H. Lim, Y. Shao, B. Li, K. M. Kwok, A. M. Seayad, A. Borgna and H. C. Zeng, *J. Mater. Chem. A*, 2023, **11**, 1593–1633.
22 J. Tian, B. Ma, S. Bu, Q. Yuan and C. Zhao, *Chem. Commun.*, 2018, **54**, 13993–13996.
23 R.-P. Ye, J. Ding, W. Gong, M. D. Argyle, Q. Zhong, Y. Wang, C. K. Russell, Z. Xu, A. G. Russell, Q. Li, M. Fan and Y.-G. Yao, *Nat. Commun.*, 2019, **10**, 5698.
24 E. C. Ra, K. Y. Kim, E. H. Kim, H. Lee, K. An and J. S. Lee, *ACS Catal.*, 2020, **10**, 11318–11345.
25 Y. Kuang and H. Li, *J. Mater. Chem. A*, 2022, **10**, 7557–7603.
26 Z. Yu, X. Lu, L. Sun, J. Xiong, L. Ye, X. Li, R. Zhang and N. Ji, *ACS Sustain. Chem. Eng.*, 2021, **9**, 2990–3010.
27 Q. Wu, L. Yang, X. Wang and Z. Hu, *Adv. Mater.*, 2020, **32**, 1–23.
28 G. H. Kim, W. H. Choi, J. W. Choi, K. H. Kim, D. G. Park, M. G. Park, M. G. Kim, H. Jang, U. H. Kim and J. K. Kang, *ACS Nano*, 2022, **16**, 6552–6564.
29 J. Wang, Y. Cui and D. Wang, *Adv. Mater.*, 2019, **31**, 1–24.
30 W. Hu, M. Zheng, B. Xu, Y. Wei, W. Zhu, Q. Li and H. Pang, *J. Mater. Chem. A*, 2021, **9**, 3880–3917.
31 Y. Boyjoo, H. Shi, Q. Tian, S. Liu, J. Liang, Z. S. Wu, M. Jaroniec and J. Liu, *Energy Environ. Sci.*, 2021, **14**, 540–575.
32 H. Huang, R. Zong and H. Li, *ACS Sustain. Chem. Eng.*, 2020, **8**, 15998–16009.
33 S. S. R. Gupta, A. Vinu and M. L. Kantam, *Chempluschem*, 2021, **86**, 259–269.
34 C. Cheng, D. Chen, N. Li, Q. Xu, H. Li, J. He and J. Lu, *J. Hazard. Mater.*, 2020, **391**, 122205.
35 Z. Xu, Y. Zhang, F. Wang, Z. Li, W. Gu, Y. Zhang and H. Xie, *Chem. Eng. J.*, 2023, **452**, 139229.
36 G. Yang, Y. Kuwahara, K. Mori, C. Louis and H. Yamashita, *Appl. Catal., B*, 2021, **283**, 119628.
37 Y. Pan, H. Li, J. Xiong, Y. Yu, H. Du, S. S. S. Li, Z. Wu, S. S. S. Li, J. Lai and L. Wang, *Appl. Catal., B*, 2022, **306**, 121111.
38 Z. Cao, P. Su, X. Wang, X. Liu, Y. Ma, C. Li, S. Ping Jiang and J. Liu, *Fuel*, 2022, **321**, 124043.
39 T. Sun, S. Zhao, W. Chen, D. Zhai, J. Dong, Y. Wang, S. Zhang, A. Han, L. Gu, R. Yu, X. Wen, H. Ren, L. Xu, C. Chen, Q. Peng, D. Wang and Y. Li, *Proc. Natl. Acad. Sci. U. S. A.*, 2018, **115**, 12692–12697.
40 Y. Chen, S. Ji, S. Zhao, W. Chen, J. Dong, W.-C. Cheong, R. Shen, X. Wen, L. Zheng, A. I. Rykov, S. Cai, H. Tang, Z. Zhuang, C. Chen, Q. Peng, D. Wang and Y. Li, *Nat. Commun.*, 2018, **9**, 5422.
41 J. Du, Y. Xin, M. Dong, J. Yang, Q. Xu, H. Liu and B. Han, *Small*, 2021, **17**, 1–7.
42 J. Gödde, M. Merko, W. Xia and M. Muhler, *J. Energy Chem.*, 2021, **54**, 323–331.
43 F. Li, S. F. Zhao, L. Chen, A. Khan, D. R. MacFarlane and J. Zhang, *Energy Environ. Sci.*, 2016, **9**, 216–223.
44 J. Lu, L. Yang, Y. Zhang, C. Wang, C. Zhang and X. S. Zhao, *ACS Appl. Nano Mater.*, 2023, **6**, 20746–20756.
45 W. Wang, C. Duong-Viet, H. Ba, W. Baaziz, G. Tuci, S. Caporali, L. Nguyen-Dinh, O. Ersen, G. Giambastiani and C. Pham-Huu, *ACS Appl. Energy Mater.*, 2019, **2**, 1111–1120.
46 Z. Liu, T. Yan, H. Shi, H. Pan, Y. Cheng and P. Kang, *ACS Appl. Mater. Interfaces*, 2022, **14**, 7900–7908.
47 Y. Fu, T. Wang, W. Zheng, C. Lei, B. Yang, J. Chen, Z. Li, L. Lei, C. Yuan and Y. Hou, *ACS Appl. Mater. Interfaces*, 2020, **12**, 16178–16185.
48 W. Zheng, C. Guo, J. Yang, F. He, B. Yang, Z. Li, L. Lei, J. Xiao, G. Wu and Y. Hou, *Carbon*, 2019, **150**, 52–59.
49 G. Yang, Y. Kuwahara, K. Mori, C. Louis and H. Yamashita, *J. Phys. Chem. C*, 2021, **125**, 3961–3971.
50 G. Yang, Y. Kuwahara, K. Mori, C. Louis and H. Yamashita, *Nano Res.*, 2021, **16**, 1–9.
51 G. Yang, Y. Kuwahara, S. Masuda, K. Mori, C. Louis and H. Yamashita, *J. Mater. Chem. A*, 2020, **8**, 4437–4446.
52 K. Li, Y. Kuwahara and H. Yamashita, *Appl. Catal., B*, 2023, **331**, 122713.
53 Z. Li, B. Li, C. Yu, H. Wang and Q. Li, *Adv. Sci.*, 2023, **2206605**, 1–53.
54 Z. Yu, N. Ji, X. Li, R. Zhang, Y. Qiao, J. Xiong, J. Liu and X. Lu, *Angew. Chem., Int. Ed.*, 2023, **62**, e202213612.
55 T. Liu, L. Zhang, B. Cheng and J. Yu, *Adv. Energy Mater.*, 2019, **9**, 1–55.
56 P. Kuang, Y. Wang, B. Zhu, F. Xia, C. W. Tung, J. Wu, H. M. Chen and J. Yu, *Adv. Mater.*, 2021, **33**, 1–9.
57 A. Fu, C. Wang, F. Pei, J. Cui, X. Fang and N. Zheng, *Small*, 2019, **15**, 1–21.
58 J. Liu, N. P. Wickramaratne, S. Z. Qiao and M. Jaroniec, *Nat. Mater.*, 2015, **14**, 763–774.

59 H. Zhang, O. Noonan, X. Huang, Y. Yang, C. Xu, L. Zhou and C. Yu, *ACS Nano*, 2016, **10**, 4579–4586.
60 Y. Li, X. F. Lu, S. Xi, D. Luan, X. Wang and X. W. (David) Lou, *Angew. Chem., Int. Ed.*, 2022, **61**, e202201491.
61 S. Li, A. Pasc, V. Fierro and A. Celzard, *J. Mater. Chem. A*, 2016, **4**, 12686–12713.
62 H. Tian, J. Liang and J. Liu, *Adv. Mater.*, 2019, **31**, 1–30.
63 Q. Yu, D. C. Li, Z. Tian, C. Zhu, C. Jiao, Q. Zhang, Y. Chen, Y. Zhu, H. Jiang, J. Liu and G. H. Wang, *Chem. Mater.*, 2022, **34**, 3715–3723.
64 J. Ye, J. Zang, Z. Tian, M. Zheng and Q. Dong, *J. Mater. Chem. A*, 2016, **4**, 13223–13227.
65 S. Cai, Z. Meng, H. Tang, Y. Wang and P. Tsiakaras, *Appl. Catal., B*, 2017, **217**, 477–484.
66 M. Karuppannan, Y. Kim, Y. E. Sung and O. J. Kwon, *J. Mater. Chem. A*, 2018, **6**, 7522–7531.
67 D. Ni, W. Sun, Z. Wang, Y. Bai, H. Lei, X. Lai and K. Sun, *Adv. Energy Mater.*, 2019, **9**, 1–10.
68 J. Chen, X. Liang, W. Liu, W. Gu, B. Zhang and G. Ji, *Dalton Trans.*, 2019, **48**, 10145–10150.
69 W. Xiong, H. Li, H. You, M. Cao and R. Cao, *Natl. Sci. Rev.*, 2020, **7**, 609–619.
70 D. Zhang, S. Shen, X. Xiao, D. Mao and B. Yan, *RSC Adv.*, 2020, **10**, 26546–26552.
71 W. Zhang, S. Yang, M. Jiang, Y. Hu, C. Hu, X. Zhang and Z. Jin, *Nano Lett.*, 2021, **21**, 2650–2657.
72 J. Du, A. Chen, X. Gao, Y. Zhang and H. Lv, *ACS Appl. Mater. Interfaces*, 2022, **14**, 11750–11757.
73 K. Min, K. Kim, H. An, Y. Go, Y. Lee, D. Lim and S. H. Baeck, *J. Power Sources*, 2022, **543**, 231849.
74 W. Ye, X. Li, B. Zhang, W. Liu, Y. Cheng, X. Fan, H. Zhang, Y. Liu, Q. Dong and M. S. Wang, *Adv. Mater.*, 2023, **35**, 1–11.
75 K. Eid, A. A. Abdelhafiz, S. Abdel-Azeim, R. S. Varma and M. F. Shibl, *Green Chem.*, 2023, **25**, 6748–6758.
76 L. Dong, Y. Li, J. Li, Y. Guan, X. Chen, D. Zhang and Z. Wang, *J. Hazard. Mater.*, 2023, **451**, 131112.
77 B. Li, Z. Ma, X. Zhang, J. Xu, Y. Chen, X. Zhang and C. Zhu, *Small*, 2023, **19**, 1–12.
78 K. Tang, L. Fu, R. J. White, L. Yu, M. M. Titirici, M. Antonietti and J. Maier, *Adv. Energy Mater.*, 2012, **2**, 873–877.
79 G. H. Wang, J. Hilgert, F. H. Richter, F. Wang, H. J. Bongard, B. Spliethoff, C. Weidenthaler and F. Schüth, *Nat. Mater.*, 2014, **13**, 293–300.
80 C. Chen, H. Wang, C. Han, J. Deng, J. Wang, M. Li, M. Tang, H. Jin and Y. Wang, *J. Am. Chem. Soc.*, 2017, **139**, 2657–2663.
81 X. Liu, P. Song, J. Hou, B. Wang, F. Xu and X. Zhang, *ACS Sustain. Chem. Eng.*, 2018, **6**, 2797–2805.
82 L. Liu, X. Sun, Y. Dong, D. Wang, Z. Wang, Z. Jiang, A. Li, X. Chen and H. Song, *J. Power Sources*, 2021, **506**, 230170.
83 F. Ma, H. Zhao, L. Sun, Q. Li, L. Huo, T. Xia, S. Gao, G. Pang, Z. Shi and S. Feng, *J. Mater. Chem.*, 2012, **22**, 13464–13468.
84 H. Sun, Y. Zhu, B. Yang, Y. Wang, Y. Wu and J. Du, *J. Mater. Chem. A*, 2016, **4**, 12088–12097.
85 W. Zhang, X. Jiang, Y. Zhao, A. Carné-Sánchez, V. Malgras, J. Kim, J. H. Kim, S. Wang, J. Liu, J. Sen Jiang, Y. Yamauchi and M. Hu, *Chem. Sci.*, 2017, **8**, 3538–3546.
86 D. Xue, D. Zhu, H. Duan, Z. Wang, Y. Lv, W. Xiong, L. Li, M. Liu and L. Gan, *Chem. Commun.*, 2019, **55**, 11219–11222.
87 X. Wei, D. Zheng, M. Zhao, H. Chen, X. Fan, B. Gao, L. Gu, Y. Guo, J. Qin, J. Wei, Y. Zhao and G. Zhang, *Angew. Chem., Int. Ed.*, 2020, **59**, 14639–14646.
88 S. Zeng, G. M. Arumugam, X. Liu, Y. Yang, X. Li, H. Zhong, F. Guo and Y. Mai, *Small*, 2020, **16**, 1–8.
89 Y. Zheng, S. Chen, K. A. I. Zhang, J. Guan, X. Yu, W. Peng, H. Song, J. Zhu, J. Xu, X. Fan, C. Zhang and T. Liu, *J. Colloid Interface Sci.*, 2022, **608**, 3168–3177.
90 Y. Chen, X. Shi, B. Lu and J. Zhou, *Adv. Energy Mater.*, 2022, **12**, 1–8.
91 B. Pan, X. Zhu, Y. Wu, T. Liu, X. Bi, K. Feng, N. Han, J. Zhong, J. Lu, Y. Y. Li and Y. Y. Li, *Adv. Sci.*, 2020, **7**, 2–7.
92 R. Li, F. Liu, Y. Zhang, M. Guo and D. Liu, *ACS Appl. Mater. Interfaces*, 2020, **12**, 44578–44587.
93 H. Chen, Y. Zhang, T. Yang, Y. Shang, Q. Zhu, S. Cao, X. Lin, S. Liu, S. Wei, B. Wei, Z. Wang and X. Lu, *Dalton Trans.*, 2022, **51**, 15883–15888.
94 W. Peng, H. Tan, X. Liu, F. Hou and J. Liang, *Energy Fuels*, 2023, **37**, 17863–17874.
95 P. Song, H. Wang, L. Kang, B. Ran, H. Song and R. Wang, *Chem. Commun.*, 2019, **55**, 687–690.
96 Y. Shang, Y. Ding, P. Zhang, M. Wang, Y. Jia, Y. Xu, Y. Li, K. Fan and L. Sun, *Chin. J. Catal.*, 2022, **43**, 2405–2413.
97 W. Peng, J. Liu, X. Liu, L. Wang, L. Yin, H. Tan, F. Hou and J. Liang, *Nat. Commun.*, 2023, **14**, 4430.
98 J. Wu, R. M. Yadav, M. Liu, P. P. Sharma, C. S. Tiwary, L. Ma, X. Zou, X. Zhou, B. I. Yakobson, J. Lou and P. M. Ajayan, *ACS Nano*, 2015, **9**, 5364–5371.
99 H. Wang, J. Jia, P. Song, Q. Wang, D. Li, S. Min, C. Qian, L. Wang, Y. F. Li, C. Ma, T. Wu, J. Yuan, M. Antonietti and G. A. Ozin, *Angew. Chem., Int. Ed.*, 2017, **56**, 7847–7852.
100 J. Xie, X. Zhao, M. Wu, Q. Li, Y. Wang and J. Yao, *Angew. Chem., Int. Ed.*, 2018, **57**, 9640–9644.
101 H. Chen, Z. Yang, C. L. Do-Thanh and S. Dai, *ChemSusChem*, 2020, **13**, 6182–6200.
102 W. Ni, Y. Xue, X. Zang, C. Li, H. Wang, Z. Yang and Y. M. Yan, *ACS Nano*, 2020, **14**, 2014–2023.
103 G. Li, Y. Qin, Y. Wu, L. Pei, Q. Hu, H. Yang, Q. Zhang, J. Liu and C. He, *Chin. J. Catal.*, 2020, **41**, 830–838.
104 C. Cheng, J. Shao, P. Wei, Y. Song, H. Li, D. Gao and G. Wang, *ChemNanoMat*, 2021, **7**, 635–640.
105 H. Cui, Y. Guo, L. Guo, L. Wang, Z. Zhou and Z. Peng, *J. Mater. Chem. A*, 2018, **6**, 18782–18793.
106 X. Duan, J. Xu, Z. Wei, J. Ma, S. Guo, S. Wang, H. Liu and S. Dou, *Adv. Mater.*, 2017, **29**, 1–20.
107 B. Qiao, A. Wang, X. Yang, L. F. Allard, Z. Jiang, Y. Cui, J. Liu, J. Li and T. Zhang, *Nat. Chem.*, 2011, **3**, 634–641.
108 Z. Zhang and D. Wang, *J. Mater. Chem. A*, 2021, **10**, 5863–5877.
109 X. He, Y. Deng, Y. Zhang, Q. He, D. Xiao, M. Peng, Y. Zhao, H. Zhang, R. Luo, T. Gan, H. Ji and D. Ma, *Cell Rep. Phys. Sci.*, 2020, **1**, 100004.
110 J. W. Sun, X. Wu, P. F. Liu, J. Chen, Y. Liu, Z. X. Lou, J. Y. Zhao, H. Y. Yuan, A. Chen, X. L. Wang, M. Zhu, S. Dai and H. G. Yang, *Nat. Commun.*, 2023, **14**, 1599.

111 X. Wang, Z. Chen, X. Zhao, T. Yao, W. Chen, R. You, C. Zhao, G. Wu, J. Wang, W. Huang, J. Yang, X. Hong, S. Wei, Y. Wu and Y. Li, *Angew. Chem., Int. Ed.*, 2018, **57**, 1944–1948.
112 X. Shi, L. N. Y. Cao, M. Chen and Y. Huang, *Chin. Chem. Lett.*, 2022, **33**, 5023–5029.
113 B. Wang, H. Cai and S. Shen, *Small Methods*, 2019, **3**, 1–14.
114 Y. Pan, R. Lin, Y. Chen, S. Liu, W. Zhu, X. Cao, W. Chen, K. Wu, W. C. Cheong, Y. Wang, L. Zheng, J. Luo, Y. Lin, Y. Liu, C. Liu, J. Li, Q. Lu, X. Chen, D. Wang, Q. Peng, C. Chen and Y. Li, *J. Am. Chem. Soc.*, 2018, **140**, 4218–4221.
115 W. Xiong, H. Li, H. Wang, J. Yi, H. You, S. Zhang, Y. Hou, M. Cao, T. Zhang and R. Cao, *Small*, 2020, **16**, 1–11.
116 S. Ma, P. Su, W. Huang, S. P. Jiang, S. Bai and J. Liu, *ChemCatChem*, 2019, **11**, 6092–6098.
117 P. Yao, J. Zhang, Y. Qiu, Q. Zheng, H. Zhang, J. Yan and X. Li, *ACS Sustain. Chem. Eng.*, 2021, **9**, 5437–5444.
118 S. Ahn, K. Park, K. R. Lee, A. Haider, C. Van Nguyen, H. Jin, S. J. Yoo, S. Yoon and K. D. Jung, *Chem. Eng. J.*, 2022, **442**, 136185.
119 X. Hai, S. Xi, S. Mitchell, K. Harrath, H. Xu, D. F. Akl, D. Kong, J. Li, Z. Li, T. Sun, H. Yang, Y. Cui, C. Su, X. Zhao, J. Li, J. Pérez-Ramírez and J. Lu, *Nat. Nanotechnol.*, 2022, **17**, 174–181.
120 L. Wang, X. Gao, S. Wang, C. Chen, J. Song, X. Ma, T. Yao, H. Zhou and Y. Wu, *J. Am. Chem. Soc.*, 2023, **145**, 13462–13468.
121 M. Jafarzadeh and K. Daasbjerg, *ACS Appl. Energy Mater.*, 2023, **6**, 6851–6882.
122 S. Liu, H. Tao, L. Zeng, Q. Liu, Z. Xu, Q. Liu and J. L. Luo, *J. Am. Chem. Soc.*, 2017, **139**, 2160–2163.
123 H. Zhang, C. He, S. Han, Z. Du, L. Wang, Q. Yun, W. Cao, B. Zhang, Y. H. Tian and Q. Lu, *Chin. Chem. Lett.*, 2022, **33**, 3641–3649.
124 D. Wei, Y. Wang, C. Dong, Z. Zhang, X. Wang, Y. Huang, Y. Shi, X. Zhao, J. Wang, R. Long, Y. Xiong, F. Dong, M. Li and S. Shen, *Angew. Chem., Int. Ed.*, 2023, **62**, e202217369.
125 Z. Zhu, Z. Li, X. Wei, J. Wang, S. Xiao, R. Li, R. Wu and J. S. Chen, *Carbon*, 2021, **185**, 9–16.
126 J. Meng, Z. Miao, J. Zhang, Z. Wang, R. Zhang, L. Xu, L. Diao, J. Zhou and S. Zhuo, *J. Alloys Compd.*, 2023, **939**, 168798.
127 K. Mori, T. Sano, H. Kobayashi and H. Yamashita, *J. Am. Chem. Soc.*, 2018, **140**, 8902–8909.
128 S. Nellaiappan, N. K. Katiyar, R. Kumar, A. Parui, K. D. Malviya, K. G. Pradeep, A. K. Singh, S. Sharma, C. S. Tiwary and K. Biswas, *ACS Catal.*, 2020, **10**, 3658–3663.
129 J. K. Pedersen, T. A. A. Batchelor, A. Bagger and J. Rossmeisl, *ACS Catal.*, 2020, **10**, 2169–2176.
130 H. J. Moon, J. M. Carrillo, J. Leisen, B. G. Sumpter, N. C. Osti, M. Tyagi and C. W. Jones, *J. Am. Chem. Soc.*, 2022, **144**, 11664–11675.
131 Z. A. Qiao, P. Zhang, S. H. Chai, M. Chi, G. M. Veith, N. C. Gallego, M. Kidder and S. Dai, *J. Am. Chem. Soc.*, 2014, **136**, 11260–11263.
132 Y. Kuwahara, H. Kango and H. Yamashita, *ACS Catal.*, 2019, **9**, 1993–2006.
133 W. Zhang, Y. Hu, L. Ma, G. Zhu, P. Zhao, X. Xue, R. Chen, S. Yang, J. Ma, J. Liu and Z. Jin, *Nano Energy*, 2018, **53**, 808–816.
134 J. Chen and L. Wang, *Adv. Mater.*, 2022, **34**, 1–30.
135 M. G. Kibria, J. P. Edwards, C. M. Gabardo, C. T. Dinh, A. Seifitokaldani, D. Sinton and E. H. Sargent, *Adv. Mater.*, 2019, **31**, 1–24.
136 N. J. Harmon and H. Wang, *Angew. Chem., Int. Ed.*, 2022, **61**, e202213782.
137 D. Gao, P. Wei, H. Li, L. Lin, G. Wang and X. Bao, *Acta Phys.-Chim. Sin.*, 2021, **37**, 2009021.
138 Y. J. Sa, C. W. Lee, S. Y. Lee, J. Na, U. Lee and Y. J. Hwang, *Chem. Soc. Rev.*, 2020, **49**, 6632–6665.
139 M. Moura de Salles Pupo and R. Kortlever, *ChemPhysChem*, 2019, **20**, 2926–2935.
140 M. R. Singh, Y. Kwon, Y. Lum, J. W. Ager and A. T. Bell, *J. Am. Chem. Soc.*, 2016, **138**, 13006–13012.
141 G. Marcandalli, A. Goyal and M. T. M. Koper, *ACS Catal.*, 2021, **11**, 4936–4945.
142 X. Wang, X. Sang, C. Dong, S. Yao, L. Shuai, J. Lu, B. Yang, Z. Li, L. Lei, M. Qiu, L. Dai, Y. Hou, Q. Zhao, J. M. P. Martirez and E. A. Carter, *Angew. Chem., Int. Ed.*, 2021, **60**, 11959–11965.
143 Q. Zhao, J. M. P. Martirez and E. A. Carter, *J. Am. Chem. Soc.*, 2021, **143**, 6152–6164.
144 N. Wang, H. Li, H. Wang, H. Yang, Z. Ren and R. Xu, *Small*, 2023, **19**, 2301469.
145 C. Yan, H. Li, Y. Ye, H. Wu, F. Cai, R. Si, J. Xiao, S. Miao, S. Xie, F. Yang, Y. Li, G. Wang and X. Bao, *Energy Environ. Sci.*, 2018, **11**, 1204–1210.
146 S. Gong, W. Wang, R. Lu, M. Zhu, H. Wang, Y. Zhang, J. Xie, C. Wu, J. Liu, M. Li, S. Shao, G. Zhu and X. Lv, *Appl. Catal., B*, 2022, **318**, 121813.
147 S. Gong, S. Yang, W. Wang, R. Lu, H. Wang, X. Han, G. Wang, J. Xie, D. Rao, C. Wu, J. Liu, S. Shao and X. Lv, *Small*, 2023, **2207808**, 1–15.
148 M. B. Ross, Y. Li, P. De Luna, D. Kim, E. H. Sargent and P. Yang, *Joule*, 2019, **3**, 257–264.
149 X. Song, H. Zhang, Y. Yang, B. Zhang, M. Zuo, X. Cao, J. Sun, C. Lin, X. Li and Z. Jiang, *Adv. Sci.*, 2018, **5**, 1–8.
150 W. Yang, J. H. Zhang, R. Si, L. M. Cao, D. C. Zhong and T. B. Lu, *Inorg. Chem. Front.*, 2021, **8**, 1695–1701.
151 X. Zheng, P. De Luna, F. P. García de Arquer, B. Zhang, N. Becknell, M. B. Ross, Y. Li, M. N. Banis, Y. Li, M. Liu, O. Voznyy, C. T. Dinh, T. Zhuang, P. Stadler, Y. Cui, X. Du, P. Yang and E. H. Sargent, *Joule*, 2017, **1**, 794–805.
152 I. M. Badawy, G. E. Khedr, A. Hafez, E. A. Ashour and N. K. Allam, *Chem. Commun.*, 2023, **59**, 7974–7977.
153 B. Ren, G. Wen, R. Gao, D. Luo, Z. Zhang, W. Qiu, Q. Ma, X. Wang, Y. Cui, L. Ricardez-Sandoval, A. Yu and Z. Chen, *Nat. Commun.*, 2022, **13**, 1–11.
154 S. H. Li, S. Hu, H. Liu, J. Liu, X. Kang, S. Ge, Z. Zhang, Q. Yu and B. Liu, *ACS Nano*, 2023, **17**, 9338–9346.
155 C. Z. Yuan, L. Y. Zhan, S. J. Liu, F. Chen, H. Lin, X. L. Wu and J. Chen, *Inorg. Chem. Front.*, 2020, **7**, 1719–1725.
156 Y. Li, S. L. Zhang, W. Cheng, Y. Chen, D. Luan, S. Gao and X. W. Lou, *Adv. Mater.*, 2022, **34**, 1–8.

157 M. Liu, S. Liu, Q. Xu, Q. Miao, S. Yang, S. Hanson, G. Z. Chen, J. He, Z. Jiang and G. Zeng, *Carbon Energy*, 2023, **5**, 1–12.
158 Yiliguma, Z. Wang, C. Yang, A. Guan, L. Shang, A. M. Al-Enizi, L. Zhang and G. Zheng, *J. Mater. Chem. A*, 2018, **6**, 20121–20127.
159 Y. Li, W. Niu, T. Chen, Y. Sun and M. Yu, *Appl. Catal., B*, 2023, **321**, 122037.
160 J. Liu, K. Yu, Q. Zhu, Z. Qiao, H. Zhang and J. Jiang, *ACS Appl. Mater. Interfaces*, 2023, **15**, 36135–36142.
161 P. P. Yang, X. L. Zhang, F. Y. Gao, Y. R. Zheng, Z. Z. Niu, X. Yu, R. Liu, Z. Z. Wu, S. Qin, L. P. Chi, Y. Duan, T. Ma, X. S. Zheng, J. F. Zhu, H. J. Wang, M. R. Gao and S. H. Yu, *J. Am. Chem. Soc.*, 2020, **142**, 6400–6408.
162 L. P. L. Gonçalves, M. Meledina, A. Meledin, D. Y. Petrovykh, J. P. S. Sousa, O. S. G. P. Soares, Y. V. Kolen'ko and M. F. R. Pereira, *Carbon*, 2022, **195**, 35–43.
163 C. Chen, Y. Li, S. Yu, S. Louisia, J. Jin, M. Li, M. B. Ross and P. Yang, *Joule*, 2020, **4**, 1688–1699.
164 H. Wu, J. Li, K. Qi, Y. Zhang, E. Petit, W. Wang, V. Flaud, N. Onofrio, B. Rebiere, L. Huang, C. Salameh, L. Lajaunie, P. Miele and D. Voiry, *Nat. Commun.*, 2021, **12**, 1–11.
165 W. Wang, W. Chu, N. Wang, W. Yang and C. Jiang, *Int. J. Hydrogen Energy*, 2016, **41**, 967–975.
166 X. Lin, S. Wang, W. Tu, Z. Hu, Z. Ding, Y. Hou, R. Xu and W. Dai, *Catal. Sci. Technol.*, 2019, **9**, 731–738.
167 J. P. O'Byrne, R. E. Owen, D. R. Minett, S. I. Pascu, P. K. Plucinski, M. D. Jones and D. Mattia, *Catal. Sci. Technol.*, 2013, **3**, 1202–1207.
168 J. Liu, Y. Sun, X. Jiang, A. Zhang, C. Song and X. Guo, *J. CO_2 Util.*, 2018, **25**, 120–127.
169 S. Wang, T. Wu, J. Lin, Y. Ji, S. Yan, Y. Pei, S. Xie, B. Zong and M. Qiao, *ACS Catal.*, 2020, **10**, 6389–6401.
170 S. A. Chernyak, A. S. Ivanov, D. N. Stolbov, S. V. Maksimov, K. I. Maslakov, P. A. Chernavskii, Y. A. Pokusaeva, A. E. Koklin, V. I. Bogdan and S. V. Savilov, *Carbon*, 2020, **168**, 475–484.
171 H. Kim, K. Mori, T. Nakano and H. Yamashita, *Adv. Funct. Mater.*, 2023, **33**, 2303994.
172 X. Li, Y. Sun, J. Xu, Y. Shao, J. Wu, X. Xu, Y. Pan, H. Ju, J. Zhu and Y. Xie, *Nat. Energy*, 2019, **4**, 690–699.
173 X. Li, K. Li, D. Ding, J. Yan, C. Wang, S. A. C. Carabineiro, Y. Liu and K. Lv, *Sep. Purif. Technol.*, 2023, **309**, 123054.
174 X. Cui, S. Shyshkanov, T. N. Nguyen, A. Chidambaram, Z. Fei, K. C. Stylianou and P. J. Dyson, *Angew. Chem., Int. Ed.*, 2020, **59**, 16371–16375.
175 Y. Dai, M. Xu, Q. Wang, R. Huang, Y. Jin, B. Bian, C. Tumurbaatar, B. Ishtsog, T. Bold and Y. Yang, *Appl. Catal., B*, 2020, **277**, 119271.
176 Y. Wang, H. Arandiyan, S. A. Bartlett, A. Trunschke, H. Sun, J. Scott, A. F. Lee, K. Wilson, T. Maschmeyer, R. Schlögl and R. Amal, *Appl. Catal., B*, 2020, **277**, 119029.
177 J. Gao, Q. Jiang, Y. Liu, W. Liu, W. Chu and D. S. Su, *Nanoscale*, 2018, **10**, 14207–14219.
178 D. Wang, Z. Xie, M. D. Porosoff and J. G. Chen, *Chem*, 2021, **7**, 2277–2311.
179 M. Cui, Q. Qian, J. Zhang, Y. Wang, B. B. Asare Bediako, H. Liu and B. Han, *Chem*, 2021, **7**, 726–737.
180 D. R. Minett, J. P. O'Byrne, S. I. Pascu, P. K. Plucinski, R. E. Owen, M. D. Jones and D. Mattia, *Catal. Sci. Technol.*, 2014, **4**, 3351–3358.
181 H. Yang, Y. Dang, X. Cui, X. Bu, J. Li, S. Li, Y. Sun and P. Gao, *Appl. Catal., B*, 2023, **321**, 122050.
182 K. Jin, C. Wen, L. Chen, Q. Jiang, X. Zhuang, X. Xu, H. Wang, L. Ma, C. Wang and Q. Zhang, *Fuel*, 2023, **333**, 126412.
183 H. Singh Malhi, Z. Zhang, Y. Shi, X. Gao, W. Liu, W. Tu and Y. F. Han, *Fuel*, 2023, **339**, 127267.
184 H. Tan, W. Si, W. Peng, X. Chen, X. Liu, Y. You, L. Wang, F. Hou and J. Liang, *Nano Lett.*, 2023, **23**, 10571–10578.
185 T. Witoon, T. Numpilai, K. Nueangnoraj, C. K. Cheng, M. Chareonpanich and J. Limtrakul, *Int. J. Hydrogen Energy*, 2022, **47**, 42185–42199.
186 P. Zhou, N. Li, Y. Chao, W. Zhang, F. Lv, K. Wang, W. Yang, P. Gao and S. Guo, *Angew. Chem., Int. Ed.*, 2019, **58**, 14184–14188.
187 S. Wei, A. Li, J. C. Liu, Z. Li, W. Chen, Y. Gong, Q. Zhang, W. C. Cheong, Y. Wang, L. Zheng, H. Xiao, C. Chen, D. Wang, Q. Peng, L. Gu, X. Han, J. Li and Y. Li, *Nat. Nanotechnol.*, 2018, **13**, 856–861.
188 Y. Chen, P. Wang, H. Hao, J. Hong, H. Li, S. Ji, A. Li, R. Gao, J. Dong, X. Han, M. Liang, D. Wang and Y. Li, *J. Am. Chem. Soc.*, 2021, **143**, 18643–18651.
189 Z. Zhang, J. Zhu, S. Chen, W. Sun and D. Wang, *Angew. Chem., Int. Ed.*, 2023, **62**, e202215136.
190 K. Mori, N. Hashimoto, N. Kamiuchi, H. Yoshida, H. Kobayashi and H. Yamashita, *Nat. Commun.*, 2021, **12**, 1–11.
191 W. Liu, P. Zhai, A. Li, B. Wei, K. Si, Y. Wei, X. Wang, G. Zhu, Q. Chen, X. Gu, R. Zhang, W. Zhou and Y. Gong, *Nat. Commun.*, 2022, **13**, 1–12.
192 R. G. Mariano, M. Kang, O. J. Wahab, I. J. McPherson, J. A. Rabinowitz, P. R. Unwin and M. W. Kanan, *Nat. Mater.*, 2021, **20**, 1000–1006.
193 L. Fan, C. Y. Liu, P. Zhu, C. Xia, X. Zhang, Z. Y. Wu, Y. Lu, T. P. Senftle and H. Wang, *Joule*, 2022, **6**, 205–220.
194 J. Wang, T. Cheng, A. Q. Fenwick, T. N. Baroud, A. Rosas-Hernández, J. H. Ko, Q. Gan, W. A. Goddard and R. H. Grubbs, *J. Am. Chem. Soc.*, 2021, **143**, 2857–2865.
195 X. Zhang, P. Wang, X. Lv, X. Niu, X. Lin, S. Zhong, D. Wang, H. Lin, J. Chen and S. Bai, *ACS Catal.*, 2022, **12**, 2569–2580.
196 B. Shao, Z. Liu, G. Zeng, Z. Wu, Y. Liu, M. Cheng, M. Chen, Y. Liu, W. Zhang and H. Feng, *ACS Sustain. Chem. Eng.*, 2018, **6**, 16424–16436.
197 H. C. Zhang, Z. X. Kang, J. J. Han, P. Wang, J. T. Fan and G. P. Sheng, *Angew. Chem., Int. Ed.*, 2022, **61**, e202200093.